Geochemistry, Geophysics, Geosystems

RESEARCH ARTICLE
10.1029/2019GC008243

Seismic Response to Injection Well Stimulation in a High-Temperature, High-Permeability Reservoir

Chet Hopp[1], Steven Sewell[1], Stefan Mroczek[1], Martha Savage[1], and John Townend[1]

[1]School of Geography, Environment and Earth Sciences, Victoria University of Wellington, Wellington, New Zealand

Key Points:
- Seismicity is induced during borehole drilling and stimulation at the Ngatamariki geothermal reservoir
- The rate of seismicity and injectivity increase is decoupled during injection well stimulation
- Stress inversions from earthquake focal mechanisms reveal distinct stress states across the reservoir

Supporting Information:
- Supporting Information S1

Correspondence to:
C. Hopp,
chet.hopp@vuw.ac.nz

Citation:
Hopp, C., Sewell, S., Mroczek, S., Savage, M., & Townend, J. (2019). Seismic response to injection well stimulation in a high-temperature, high-permeability reservoir. *Geochemistry, Geophysics, Geosystems*, *20*, 2848–2871. https://doi.org/10.1029/2019GC008243

Received 29 JAN 2019
Accepted 13 MAY 2019
Accepted article online 20 MAY 2019
Published online 20 JUN 2019

Abstract Fluid injection into the Earth's crust can induce seismic events that cause damage to local infrastructure but also offer valuable insight into seismogenesis. The factors that influence the magnitude, location, and number of induced events remain poorly understood but include injection flow rate and pressure as well as reservoir temperature and permeability. The relationship between injection parameters and injection-induced seismicity in high-temperature, high-permeability reservoirs has not been extensively studied. Here we focus on the Ngatamariki geothermal field in the central Taupō Volcanic Zone, New Zealand, where three stimulation/injection tests have occurred since 2012. We present a catalog of seismicity from 2012 to 2015 created using a matched-filter detection technique. We analyze the stress state in the reservoir during the injection tests from first motion-derived focal mechanisms, yielding an average direction of maximum horizontal compressive stress (S_{Hmax}) consistent with the regional NE-SW trend. However, there is significant variation in the direction of maximum compressive stress (σ_1), which may reflect geological differences between wells. We use the ratio of injection flow rate to overpressure, referred to as injectivity index, as a proxy for near-well permeability and compare changes in injectivity index to spatiotemporal characteristics of seismicity accompanying each test. Observed increases in injectivity index are generally poorly correlated with seismicity, suggesting that the locations of microearthquakes are not coincident with the zone of stimulation (i.e., increased permeability). Our findings augment a growing body of work suggesting that aseismic opening or slip, rather than seismic shear, is the active process driving well stimulation in many environments.

Plain Language Summary When industries inject fluid into the Earth, oftentimes earthquakes are the result. Although this presents a hazard to nearby infrastructure and populations, studying these events helps us understand how fluid is moving underground and the processes that create earthquakes. In this paper, we describe over 9,000 earthquakes that occurred over a 4-year period at a geothermal field on the North Island of New Zealand. The details of where and when they occurred and how big they were give us clues about fractures ~3,000-m underground and therefore how easily fluid can move from point A to point B underground. We focus on two wells where operators injected cold water (~20 °C) at high pressure to try to open fractures in the reservoir. This would allow them to extract and reinject more fluid and therefore produce more power. We found that, while some of these operations triggered earthquakes, the amount of fluid that could be pumped into the ground was not related to the number of earthquakes. This means that, in the future, companies may be able to design injection operations so that they achieve their goal of opening fractures underground, without also generating large earthquakes.

1. Introduction

In recent years, the number of recorded cases of injection-induced seismicity has grown dramatically with the proliferation of industrial activities such as wastewater disposal and enhanced geothermal systems (EGS; Ellsworth, 2013). In many cases, most notably in the central United States and Europe, these activities have induced events that caused damage to local infrastructure and even a number of injuries (e.g., Deichmann & Giardini, 2009; Hsieh & Bredehoeft, 1981; Keranen et al., 2013; Ge et al., 2019). However, these injections also offer valuable insight into seismogenesis, which may help to better manage future injection-induced seismic hazard. While most case studies have addressed low-temperature, high-permeability reservoirs such as the Arbuckle group in Oklahoma (e.g., Langenbruch & Zoback, 2016) or medium-temperature, low-permeability reservoirs targeted at EGS sites (e.g., Deichmann & Giardini, 2009; Evans et al., 2005), here we present a case of induced seismicity related to injection operations in the high-temperature,

high-permeability Ngatamariki geothermal reservoir. Though seismicity associated with such reservoirs has been well documented for decades (e.g., at The Geysers field in California), most studies have needed to consider simultaneous injection from multiple wells with long histories of injection, thereby complicating the relationship between induced seismicity and injection parameters such as flow rate and wellhead pressure (WHP; e.g., Allis, 1982; Martínez-Garzón et al., 2014; Martínez-Garzón et al., 2017; Kwiatek et al., 2015). Here we present a much simpler case study involving multiple injections isolated from one another in both space and time.

The aim of underground fluid injection is typically to dispose of unwanted fluids or to increase permeability at depth (Ellsworth, 2013; Grant & Bixley, 2011). In the geothermal industry, an increase in permeability allows for more fluid to be injected or produced, thus reducing the number of wells required per unit of electrical generation. Fluid injection drives a number of processes that contribute to the occurrence of seismicity, including pore fluid pressure increases, reservoir volume changes (due to injection or extraction of fluid), reservoir temperature decreases and chemical changes to fracture surfaces (Majer et al., 2007). The conditions under which these processes induce seismicity and the relationship between seismic or aseismic slip and reservoir properties such as fracture permeability remain unclear (Amann et al., 2018; Das & Zoback, 2011, and references therein). Unraveling these potential relationships is important in order to better plan future geothermal resource development and has implications for deep injection operations and the understanding of seismogenesis in general.

The Ngatamariki geothermal field in the central Taupō Volcanic Zone of New Zealand is a convenient place to study induced seismicity. Prior to our study period, which extends from June 2012 to the end of 2015, the development of the Ngatamariki resource had been limited to resource exploration in the 1980s followed by the drilling of three deep exploration wells (NM05, NM06, and NM07 to ~3-km depth) in the 2000s (Chambefort et al., 2016). The start of injection operations in 2012 represented the first large-scale fluid injection into the undisturbed, high-temperature (~280 °C) Ngatamariki reservoir (Bignall, 2009). Fluid injection at three of the four major injection wells (NM08, NM09, and NM10) was undertaken in advance of the Ngatamariki power plant's commissioning in 2013. Pressure and flow rate during each of these operations was well recorded (5-min resolution). As each operation occurred in isolation, the task of relating temporal and spatial patterns of microseismicity to injection parameters for a specific well was straightforward. Seismic data were recorded throughout these injections, enabling us to detect and precisely locate a large number of induced microearthquakes.

In the Ngatamariki case, the objectives of individual injection operations differed. Generally, these injections can be divided into three categories: cold-water stimulation, injection testing, and unintended fluid losses during drilling. Cold-water stimulation is a process intended to increase the permeability in a given well and which is thought to be driven by the thermal contraction of reservoir rocks (Grant et al., 2013). Injection testing, while often conducted in conjunction with stimulation, is aimed at determining the injectivity index of a well, which is normally defined as the ratio of flow rate to wellhead pressure. This parameter is then used as an indicator of a well's bulk permeability and to predict injection well performance once a power plant begins operation. Fluid losses during drilling are generally unintended and result from the escape of drilling fluid into the formation as the well is drilled. Each of these scenarios occurred at Ngatamariki prior to the startup of the 82 MWe ("megawatts electrical") power plant in April of 2013. As we show below, the rate, location, and magnitude of microseismicity associated with each individual injection operation were distinct, demonstrating differences in local geology, near-well permeability, fluid injection rate, history of injection, and the temperature and chemistry of the injected fluid in each well.

In this paper, we construct a catalog of induced seismicity at Ngatamariki and compare the characteristics of seismicity to flow rate, pressure, and injectivity index measured during three phases of injection prior to the startup phase of the Ngatamariki power plant. The temporal isolation of each phase of injection allows us to relate near-well seismicity to high-resolution injection parameters without contamination from multiple, concurrent injections. Given that the Ngatamariki reservoir occupies the upper end of both the temperature and permeability continuum, the injection-seismicity relationship here serves as a useful comparison to results from lower-temperature and lower-permeability settings elsewhere. Therefore, our results help to distinguish the importance of reservoir permeability and temperature in forecasting the extent and magnitude of induced seismicity during future injection operations.

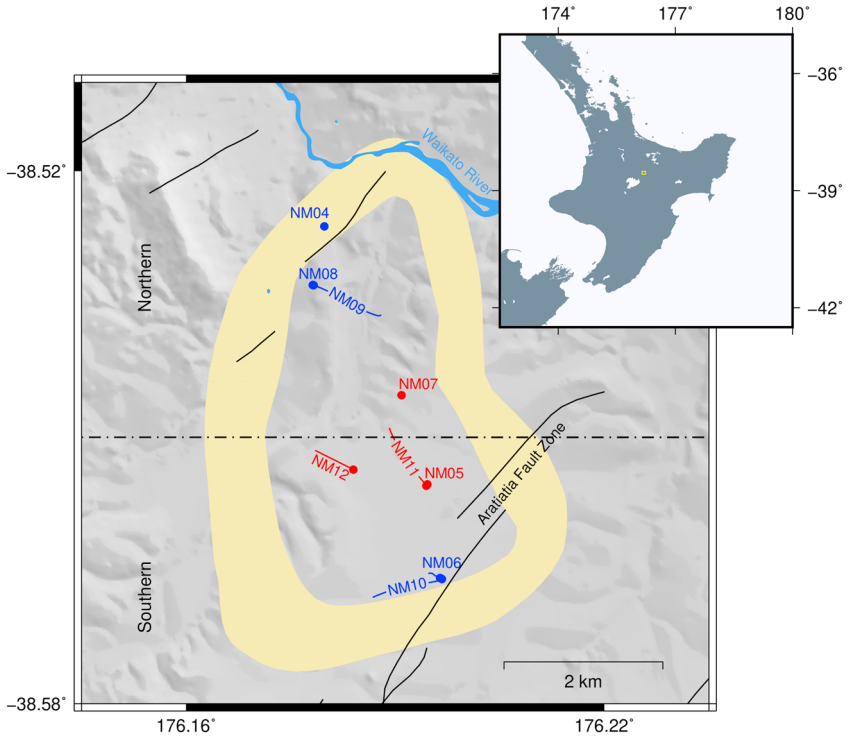

Figure 1. Overview of the Ngatamariki geothermal field. Injection wells are shown in blue, production wells in red with dots representing the wellhead, and lines showing the surface projection of the well tracks at depth. Wells NM04, NM08, NM05, and NM07 are near vertical and, therefore, appear only as dots in the figure. Active faults from the GNS Science Active Faults Database (Langridge et al., 2016) are shown in black. The most likely boundary of the deep resource as published by Boseley et al. (2010) based on magnetotelluric surveys is shown in yellow. The northern and southern portions of the field, as referred to in this work, are divided at −38.55° latitude and labeled here.

1.1. Geological and Geophysical Setting

The Ngatamariki geothermal field is located in the central Taupō Volcanic Zone (TVZ) on the North Island of New Zealand, approximately 17 km north of the town of Taupō (Figure 1). Ngatamariki is a high-temperature, liquid-dominated, and naturally fractured system (280 °C at depths exceeding 1,000 m) that measures roughly 5.5 km from north to south and 3 km from east to west (Bignall, 2009; Chambefort et al., 2014). The reservoir is hosted in a succession of volcaniclastics known as the Tahorakuri formation, which exhibits significant lateral heterogeneity (Chambefort et al., 2014). In the south, the deeper portions of the reservoir (<2,000 m below sea level [bsl]) are hosted in the Rotokawa Andesite. In this part of the field, the Rotokawa Andesite overlies greywacke basement, which has been encountered in only one well (NM06) at 3,012 m bsl (Chambefort et al., 2014). The geologic structure of the southern end of the field, between the central production wells and injection wells NM06 and NM10, is dominated by the active, NE-SW striking Aratiatia Fault Zone (Figure 1). Reservoir tracer tests have demonstrated the presence of high permeability between injection well NM10 and production well NM05 along an Aratiatia Fault Zone-related structure (Buscarlet et al., 2015). In the north, in the vicinity of injection wells NM08 and NM09, the reservoir geology is dominated by a shallow intrusive body (<2,000 m bsl), the presence of which was confirmed by drill cuttings and core in NM08, NM09, and NM04 (Bignall, 2009; Chambefort et al., 2014). The intrusive body lacks appreciable permeability itself, but it is enveloped by a highly fractured damage zone that was encountered in wells NM08 and NM09 (Clearwater et al., 2015). Given the low permeability of the reservoir matrix, typical of the TVZ (Sibson & Rowland, 2003), fluid flow is controlled by fractures and faults. Regionally, faults follow a NE-SW structural trend and borehole image logs at Ngatamariki indicate mostly NE-SW oriented fractures within the reservoir, with some variability with depth in certain wells (Bignall, 2009; Massiot et al., 2012, 2015).

1.2. Mechanisms of Microseismicity and Permeability Enhancement

The main driver of microseismicity at Ngatamariki is the injection of cool (<100 °C) fluid into the hot (~280 °C) reservoir. It is generally accepted that fluid injection increases the pore fluid pressure near an

injection well, lowering the effective normal stress and inducing slip on suitably oriented fractures with respect to the local stress field (e.g., Ellsworth, 2013; Langenbruch et al., 2018; Zoback & Harjes, 1997). At every point on a fracture or fault, there is a specific pore pressure increase, ΔP_{crit}, that will lower the shear strength of the fracture/fault to the point of failure (Wiprut & Zoback, 2000). Injection, especially in high-temperature geothermal reservoirs, also introduces a thermal gradient in the host rock. This may produce enough stress to induce tensile failure or opening of preexisting fractures (Martínez-Garzón et al., 2014). It also reduces stress locally through thermoelastic contraction of the rock matrix, bringing the reservoir fracture network closer to or further from failure depending upon the direction of fluid flow relative to the orientation of the in situ stress state (Jeanne et al., 2014). Furthermore, as geothermal fluid moves through a formation, it may dissolve minerals (e.g., calcite) out of, or precipitate minerals into, fractures. Though less well understood, this effect may play a large part in creating or destroying permeability through opening or sealing of fractures that would be likely to fail (Clearwater et al., 2015). Injection and extraction of large quantities of fluid can also significantly change the volume of the reservoir, poroelastically influencing the distribution of stress and often leading to reservoir compaction, surface subsidence, and seismicity (Bromley et al., 2013; Segall, 1989; Segall & Fitzgerald, 1998). Finally, slip itself (both seismic and aseismic) transfers stress onto nearby fractures and faults, an effect that has been shown to play a role in triggering subsequent seismicity in geothermal fields and elsewhere (Catalli et al., 2016; Schoenball et al., 2012).

The relationship between seismicity and permeability has been widely studied in laboratory settings (e.g., Lee & Cho, 2002, and references therein). When slip occurs on a new or preexisting fracture, asperities become offset and the permeability of that fracture increases (an effect known as self-propping), which depends on the length of the slip vector and the roughness of the fault surface (Esaki et al., 1999; Fang et al., 2017; Ishibashi et al., 2018). It is commonly assumed that the permeability increase observed during injection is the result of seismic fault slip, a correlation which has been modeled for EGS cases previously (e.g., Baisch et al., 2010). It is important to note, however, that a large percentage of the permeability enhancement that accompanies well stimulation may be aseismic, as has been directly observed during a decameter-scale injection experiment described by Guglielmi et al. (2015) and in seismic data recorded during hydraulic fracturing (Das & Zoback, 2011). Further evidence of aseismic slip has been inferred at the high-temperature Salton Sea geothermal field in southern California from a combined geodetic and seismic data set (Wei et al., 2015). Riffault et al. (2018) have also demonstrated that, in some cases, permeability enhancement may not be coupled to detectable seismic slip at all. In the context of high-temperature geothermal reservoirs, thermal stresses induced near the wellbore may govern most of the permeability enhancement observed during well stimulation through the expansion of permeable zones (Grant et al., 2013; Siega et al., 2014), a process that may be aseismic.

At Ngatamariki, the dominant processes driving microseismicity have previously been interpreted to be thermal and pore fluid pressure changes (Grant et al., 2013; Sherburn et al., 2015). The Ngatamariki power plant reinjects most of the extracted fluid, and as a result, the pressure drawdown observed across the field is minor (~0.2 MPa). This suggests that reservoir compaction plays a small role in inducing local stress changes in this case (Quinao et al., 2017). However, at nearby fields that have been produced for much longer than Ngatamariki, significant pressure drawdown-related subsidence has occurred (Allis, 2000). Poroelestic stress transfer resulting from rock matrix contraction and slip on fractures cannot be ruled out as possible factors affecting reservoir permeability and induced seismicity. However, in the case of the NM08 and NM10 injection tests and NM09 stimulation A (introduced below), the injection of river water also renders unlikely the precipitation of minerals as a possible mechanism of permeability change. This cannot be said of the brine injected during the second phase of NM09 stimulation.

1.3. Ngatamariki Power Plant Operations

Mercury NZ Ltd., then known as Mighty River Power, began generation of electricity at Ngatamariki in October 2013 with the commissioning of an 82-MWe binary power plant. The company was granted a consent for production of 60,000 tons of geothermal fluid per day, approximately 98% of which is currently reinjected into the deep reservoir at between 1,000- and 3,000-m depths. The reinjected fluid is allocated nearly evenly between the injection wells to the north (NM08 and NM09) and those to the south (NM06 and NM10; Buscarlet et al., 2015; Clearwater et al., 2015). Between June 2012 and April 2013, three of the four main injection wells were subject to some form of injection operation (Table 1). Cold-water stimulation of NM08 took place between 8 June and 10 July 2012 using ~10 °C river water. Well NM10 was drilled between late May and early August 2012, using fluid consisting almost entirely of river water, and significant fluid

Table 1
Table Summarizing the Injection Operations Presented Here, All of Which Were Undertaken Prior to Plant Startup at Ngatamariki

Operation	Zone	Start	End	Injectate	Max Q (t/hr)	Max Pres. (MPa)
NM08 stimulation	Northern	2012-06-08	2012-07-10	River water	175	2.63 (WHP)
NM10 drilling	Southern	2012-05-25	2012-08-11	Drilling fluid	141	N/A
NM10 stimulation	Southern	2012-09-01	2012-09-23	River water	201	9.3 (DHP)
NM09 stimulation A	Northern	2012-12-14	2013-01-04	River water	170	0.2 (WHP); 15.3 (DHP)
NM09 stimulation B	Northern	2013-02-13	2013-03-06	Brine	152	0.3 (WHP); 13.0 (DHP)

Note. The maximum pressures reported in the final column are for wellhead pressure (WHP), downhole pressure (DHP), or both where present. Q denotes flow rate in tons per hour. Date is formatted as YYYY-MM-DD.

losses occurred after 13 July. After the completion of drilling, NM10 injection testing was conducted on 1–23 September. NM09 was drilled between September and early November 2012, with subsequent injection testing occurring in two phases. The first took place between 14 December 2012 and 4 January 2013, and the second lasted from 13 February to 6 March 2013 (Clearwater et al., 2015), the latter using geothermal brine instead of river water. This paper focuses on the cold-water stimulation of NM08, drilling and cold-water stimulation of NM10, and cold-water stimulation of NM09.

In March 2013, as the plant was being brought online, Mercury began reinjection of brine into all injection wells including NM06, which had been drilled several years earlier. Geothermal brine at Ngatamariki is injected at a temperature of approximately 90 °C. However, at times when production exceeded plant intake capacity during the early stages of plant startup, some brine bypassed the plant and was injected at temperatures of as much as 150 °C (Clearwater et al., 2015). Over the following year, injection at Ngatamariki reached a stable level of ~1,000 tons per hour (t/hr; one t/hr is equivalent to 0.28 L/s) at NM09, ~200 t/hr at NM08, and ~800 t/hr at NM06. NM10 was initially an active injector, but due to the strong hydraulic connectivity between it and the production well NM05, it was phased out by mid-2015 (Buscarlet et al., 2015).

2. Data

The Mercury seismic network covers an area roughly 30 km (N-S) by 15 km (E-W) with the bulk of the stations occupying an area 15 km (N–S) by 7 km (E-W) centered around the Rotokawa and Ngatamariki geothermal areas (Figure S1 in the supporting information). The majority of the instruments are either 4.5-Hz Geospace GS-11D short-period geophones or Lennartz LE-3DLite 1-Hz instruments, but the network also includes stations operated by Contact Energy (THQ2 and ARAZ) at the Wairakei and Tauhara geothermal fields and nearby stations operated by the national seismic network, GeoNet (WPRZ, PRRZ, HRRZ, and ALRZ; Table S1 in the supporting information). The GeoNet stations are broadband instruments with the exception of WPRZ, which is a 1-Hz LE-3Dlite. From the beginning of 2012 until the end of 2015, the number of operational stations varied between 15 and 29. Sites NS12, NS13, and NS14 in the middle of the Ngatamariki network are 2-Hz borehole instruments installed at depths of between 200 and 514 m below the ground surface (Figure S1 in the supporting information).

The initial earthquake catalog for this study was provided by GNS Science under contract to Mercury. The waveform data were collected roughly every 3 months from Mercury's data loggers and supplemented by data from nearby GeoNet stations. GeoNet data were sampled at 100 Hz, while the Mercury network data were sampled at 200 Hz. For much of this study, all data were resampled at 50 Hz to reduce computational costs. Events in the initial GNS Science earthquake catalog had been automatically detected and located with the *SeisComP3* software package (Weber et al., 2007). We filtered the catalog to include only these events within or immediately adjacent to the field boundaries at Ngatamariki, leaving a total of 1,171 microearthquakes of local magnitudes between 0.26 and 3.17. Magnitude-distance corrections were computed using events recorded by both the Mercury seismic network and GeoNet. The calibration factor for a given event station distance, A_0, was calculated from $M = \log_{10}A - \log_{10}A_0$, where A is the event amplitude at the station and M the GeoNet calculated magnitude. A_0 was averaged across all stations in the Mercury network for all events recorded by GeoNet to obtain the final calibration factors. A final, static correction factor of +0.32 was applied to the Mercury magnitudes to bring them into agreement with GeoNet-calculated magnitudes (Figure S2). We relocated these events using the double-difference relocation software of Waldhauser (2000), the results of which are shown relative to the seismic network in Figure S3 (supporting

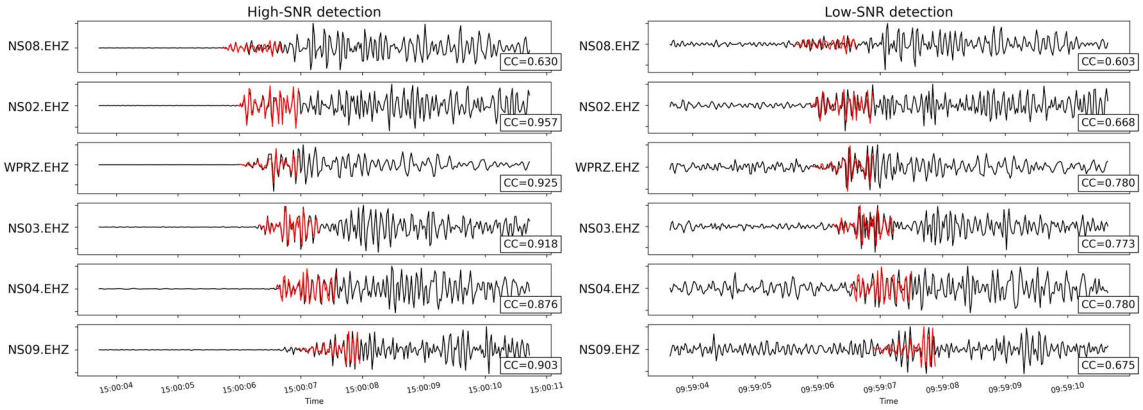

Figure 2. Example detections of two events by template 2012sora469246 (signal-to-noise ratio of ~50 and ~3, respectively). The 1-s templates (in red) are overlain on 10 s of continuous data around the time of detection (black). The M_L 0.62 template event occurred on 22 June 2012 and detected mostly events that occurred during the stimulation of well NM08 between 6 June and early July. The detection on the left represents a detection of a separate, yet highly similar, template event (template 2012sora469256) which occurred approximately 10 min after the template event shown here. The detection on the right is a newly detected event. SNR = signal-to-noise ratio.

information). Production and injection well locations as well as flow rates and pressures at each well were provided by Mercury.

3. Methods

3.1. Matched-Filter Detection

The small magnitudes of events, high levels of anthropogenic noise, and highly attenuating geology at Ngatamariki make detecting microearthquakes difficult. One way to address this difficulty is to use a waveform correlation-based detection technique. Correlation-based detection, otherwise referred to as matched-filter detection, offers improved performance over traditional, amplitude-based techniques due to its ability to detect signals in noisy data and when multiple events are closely spaced in time (Gibbons & Ringdal, 2006; Shelly et al., 2007). This significantly increases the number of events detected without drastically increasing the rate of false detections and is ideal for monitoring microseismicity. Such a technique is ideally suited to areas of geothermal power generation, which are characterized by numerous noise sources and dense clusters of small seismic events.

Matched-filter earthquake detection relies on waveform cross-correlation of a known earthquake signal or signals, referred to as templates, with continuously recorded seismic data. The following equation, which we use for this study, describes normalized cross-correlation in the time domain (Chamberlain et al., 2017)

$$R(x) = \frac{\sum_{x'=0}^{x+w_x}(T'(x') \cdot I'(x+x'))}{\sqrt{\sum_{x'=0}^{x+w_x}(T'(x')^2 \cdot \sum_{x'=0}^{x+w_x} I'(x+x')^2}} \quad (1)$$

Here I' represents the continuous seismic data of interest and T' represents the template earthquake. x represents the sample in the continuous data between sample 0 and sample $(N_x - w_x)$, where N_x is the length of the continuous data being searched and w_x is the length of the template. x' is the position within the window over which the correlation is being calculated.

Each of 1,171 events taken from the GNS Science catalog outlined in section 2 was used as a template event (Figure S3). Each template consists of 1-s-long waveforms, starting 0.1 s before the P phase arrival on the vertical channel at each station on which a P pick was made (e.g., red waveforms in Figure 2). Horizontal channels are not used due to the large uncertainties for the automatic S picks in the GNS Science catalog. However, a length of 1 s ensures that both P and S arrivals are included in the vertical channel template for each event due to the short travel times. A length of 1 s also omits most of the coda, which is incoherent for even highly similar sources. This effect is especially apparent at Ngatamariki, due to the highly fractured reservoir, large variations in the volcanic geology (i.e., welded ignimbrites and ashfall deposits), and surface heterogeneity. After applying an antialiasing filter, waveforms were sampled at 50 Hz and filtered from 3.0 to

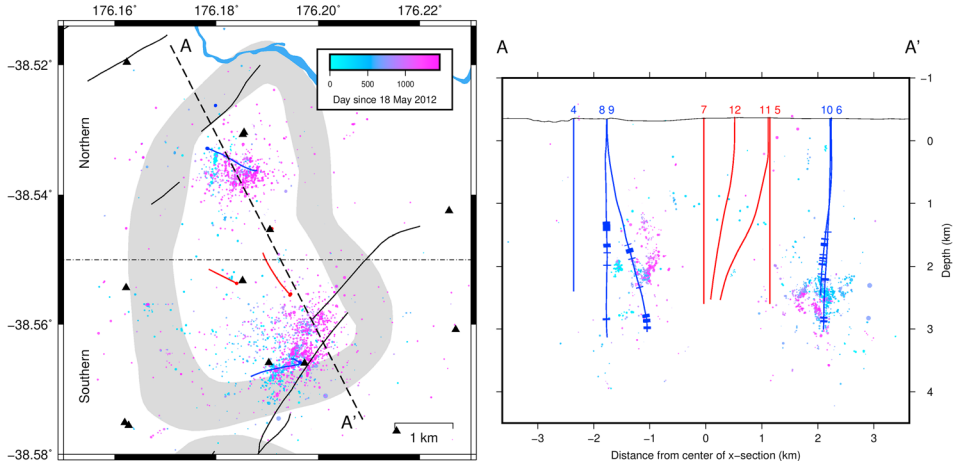

Figure 3. Relocated Ngatamariki seismic catalog for May 2012 through November of 2015 using the double-difference relocation method of Trugman and Shearer (2017). Production (red) and injection (blue) wells are shown with circles representing the wellhead and lines representing the surface projection of the wellbore at depth. In cross section, the major feed zones in each injection well are shown as wide, blue rectangles. Events are colored by the date on which they occurred and scaled by their magnitude ($M_{max} = 3.1$). Teal corresponds to the start of the data set and pink to the end. Black triangles denote locations of seismic stations. The northern and southern portions of the field are divided by a dash-dotted line and labeled.

20.0 Hz to include the high corner frequencies of events with event station distances of <5 km. Continuous seismic data were processed in an identical manner to the templates for the matched-filter routine.

To generate detections, event templates were cross-correlated with continuous data at a rate of 50 samples per second. At each sample, the cross-correlation coefficients for each channel of data were summed to create the network detection statistic (Shelly et al., 2007). A detection was recorded whenever the detection statistic exceeded a threshold value, which in this case was defined as the daily median absolute deviation of the detection statistic multiplied by 8 (as suggested by Shelly et al., 2007). We refer to a template event, along with all of its associated detections, as a family.

We split all families into separate groups for northern and southern Ngatamariki before removing duplicate detections. This allows us to account for simultaneous seismicity within both clusters, which we would expect in response to simultaneous injection at the two distinct injection zones. However, the separation of the two clusters prior to duplicate removal introduces the possibility of double-counting events detected by two templates if both templates are located in separate spatial clusters. We have checked for this case explicitly and have eliminated these cases in the final catalog presented here.

Within each spatial cluster, duplicate removal was conducted by looping through all detections in order of descending detection statistic and removing detections within a user-defined time buffer of 2 s. We adopted 2 s for the time buffer after a visual review of template events revealed numerous cases of near-repeating seismicity with interevent times of 3–5 s.

Visual inspection of a subset of the detection waveforms showed that false detections occurred at a rate of approximately 1–3 false detections per day. However, the quantity of detections makes visual review of the entire detection catalog impracticable. Therefore, we employ a sequence of thresholds based on the cross-correlation between the template and detected waveforms to exclude lower-quality events. We do this during both the location and magnitude calculations detailed below. Applying these correlation cutoffs has the effect of suppressing false detections in the final catalog that we use in this analysis. As a final quality assurance step, we visually inspected hundreds of waveforms from the final catalog in order to manually pick first motion polarities and did not encounter a false detection.

3.2. Detection Location

After removing duplicate detections, *P* picks for each of the newly detected events were made at each channel included in the template. For each station, template waveforms were correlated with the detected waveform over a 0.2-s window centered on the detection time. Picks were recorded at the time corresponding to the highest correlation value within that window. However, if the correlation value of the template and detected

waveform fell below 0.4, the pick was discarded. We retained all events with more than five picks and discarded those with five or fewer. For the retained events, we then made automatic *S* picks (Mroczek et al., 2016) using the method developed by Diehl et al. (2009) and modified by Castellazzi et al. (2015). These events were then located with the nonlinear location program *NonLinLoc* (Lomax et al., 2014) using a preliminary 1-D model computed with *VELEST* (Kissling et al., 1994; Sewell et al., 2017; Table S2). As a final step, the entire catalog was relocated using the double-difference relocation program *GrowClust* (Trugman & Shearer, 2017) with differential pick times generated using the Python package *hypoDDpy* (Krischer, 2015). The final double-difference relocations are shown in Figure 3.

3.3. Magnitudes

To compute the magnitude of the events detected by the matched filter, we used the method described by Shelly et al. (2016). This technique uses pairwise relative amplitudes between a template event and each of its detections to compute relative moments. This approach computes the relative amplitude, α, as

$$\alpha = \frac{v[2]}{v[1]} \tag{2}$$

where $v[2]$ and $v[1]$ are the second and first elements, respectively, of the first row of the 2×2 matrix V' in

$$M = U\Sigma V' \tag{3}$$

describing the singular value decomposition of a data matrix, M, containing both the template and the detected waveform on a single channel. The rows of V' are the right singular vectors that map the weight of the left singular vectors, U, to the original data vectors. Because the template and detected waveforms in the data matrix are inherently similar, the first left singular vector, U_0, should describe only a difference in amplitude between template and detection. The relative amplitude between the two events can therefore be estimated as the ratio of the second and first elements, $v[2]$ and $v[1]$, of the first row of V'.

We calculated relative amplitudes only when the cross-correlation coefficient between the template and detection exceeded 0.6 at any given station. Again, we note that template events only contain waveforms for the vertical channels. For those events recorded by a minimum of four stations exceeding the correlation threshold, we calculated the relative moment as the median of the relative amplitudes, following Shelly et al. (2016). We note that, because the relative amplitudes are calculated from two waveforms recorded at the same station, there is no need to remove the instrument response.

This approach has proven to be more robust in the presence of relatively dissimilar waveforms than the method of Rubinstein and Ellsworth (2010), which assumes high-correlation coefficients between all events in a family (e.g., $\geq$0.85). In the Ngatamariki case, scattering and attenuation effects produce waveforms exhibiting lower degrees of similarity than typical repeating or near-repeating seismicity (e.g., along the San Andreas; Rubinstein & Ellsworth, 2010).

We used the GNS Science M_L (as described in section 2) to calibrate the relative moment calculations from the method above and produce M_L estimates for matched-filter detections. This was done by first converting the template local magnitudes to moment magnitudes using the scaling relationship

$$M_L = 0.88M_w + 0.73 \tag{4}$$

determined for locally detected, shallow New Zealand earthquakes (Ristau, 2009) and then converting to seismic moment using the equation (Hanks & Kanamori, 1979)

$$M_w = 2/3\log_{10}M_0 - 9 \tag{5}$$

Knowing the relative moment of the template event from the procedure outlined above, we then determined the relationship between the relative moments and actual moment which allowed us to convert relative moments to M_w and then back to M_L using the relationship of Ristau (2009).

3.4. Focal Mechanisms and Stress Inversion

Focal solutions for selected events were calculated from *P* arrival polarities using the Bayesian focal mechanism determination program of Walsh et al. (2009). Here, we present only focal mechanism solutions for the 86 events that occurred prior to plant startup in March 2013 and that had sufficiently high signal-to-noise

ratio for the arrival polarities to be manually picked. These focal mechanisms were then used to invert for the stress parameters and the direction of maximum horizontal compressive stress (S_{Hmax}) within the northern and southern clusters separately, using the methodologies of Arnold and Townend (2007) and Lund and Townend (2007).

4. Results

4.1. Matched-Filter Detection

Starting with the 1,171 template events in the automatically detected catalog provided by GNS Science, we added 76,286 detections after matched filtering, creating a total catalog of 77,457 events. At Ngatamariki, seismicity in both the GNS Science catalog and the matched-filter catalog falls into two spatial groups, which we refer to hereafter as the northern and southern clusters. We delineate the templates broadly by latitude whereby the northern cluster contains all templates located north of −38.55° and the southern cluster contains all templates to the south (Figure 1). The northern cluster consists of 432 template events, which generated 25,482 detections. The southern cluster consists of 739 template events, which generated 50,804 detections. Two representative detections for a single template from the northern cluster are shown in Figure 2.

4.2. Event Location

We calculated preliminary locations for 41,114 events of the 77,457 total detections. Of the 5,981 of these events for which we calculated magnitudes, we were able to relocate 2,554. Given that events detected by the matched-filter method are, by design, similar to the template event that detected them, the locations of the detections should closely match the locations of the template events. Figures 3 and S3 show the detected and template events, respectively, plotted with depth and colored by their date of occurrence (blue for earlier in the data set and pink for later).

In northern Ngatamariki, most events occur within a cloud of seismicity extending from ~1,500 to 2,500 m bsl. This cloud is spatially coincident with the dominant feed zones in well NM09 at between ~1,600 and 1,800 m bsl (Figure 3). The injection rate during normal power plant operation is roughly 1,100 t/hr into NM09 and ~300 t/hr into NM08. During the stimulation of NM08, seismicity occurred within a narrow, NW-dipping band at ~2,200 m bsl. These events likely define the extent of a suitably oriented fault that was activated during the treatment and which is discussed in more detail in section 5.1.1.

In the south of the field, seismicity occurred in a cluster at depths of ~2,000–3,000 m bsl, elongated in the NE-SW direction and subparallel to the strike of the Aratiatia Fault Zone (Figure 1). These depths coincide with the depths of the major feed zones in injection well NM06, not with the feed zones in NM10. Over the entire 4-year data set, seismicity in the southern injection zone migrates from SW to NE. We attribute this migration to a shift in injection strategy in this part of the field. Originally, injection was split equally between NM10 and NM06, but by 2015 all injection in the south was into NM06 due to rapid returns from NM10 to production well NM05 (Buscarlet et al., 2015).

The depth of seismicity in southern Ngatamariki is greater, on average, than in the north. In the south, hypocentral depths correspond to the depth of the Rotokawa Andesite and the lower Tahorakuri Formation (Chambefort et al., 2014) with shallower seismicity nearer to the production wells than the injection wells. In the north, below ~2,000 m bsl, the reservoir is dominated by the intrusive body (Chambefort et al., 2014). The seismicity depth cutoff near both injection zones is likely related to the depth of permeable zones in the wells (Halwa, 2013a, 2013b; Massiot et al., 2012). In the north, relatively little seismicity occurs within the bounds of the impermeable intrusive body and in the south most events are confined to the Rotokawa Andesite, which is known to be heavily fractured (Halwa, 2013b).

Bottomhole temperatures for the northern injection wells reach ~280 °C, and production well NM07 reaches almost 290 °C. In contrast, the maximum temperatures in the southern injection zone reach only ~260 °C and are located away from the main upflow in the field (between NM07 and NM08/09; Chambefort et al., 2016). While these temperatures could be interpreted to be near the brittle-ductile transition for quartz-bearing rock (e.g., Scholz, 1988), this is unlikely given that seismicity at the nearby (and lithologically similar) Rotokawa geothermal field occurs in host rock with measured temperatures in excess of 330 °C (Sewell et al., 2015). We also caution against the use of microseismic hypocenters in defining the depth of significant permeability for constraining the base of reservoir models, partly due to uncertainties in the hypocentral depth (~200 m). In addition, recent results have shown that a significant portion of induced

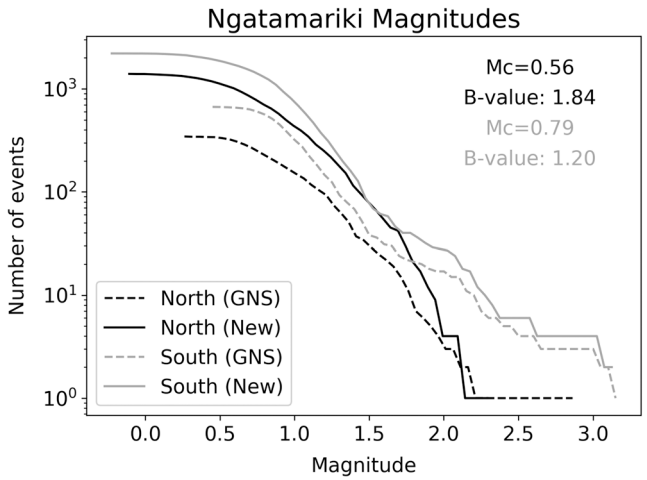

Figure 4. Cumulative frequency-magnitude distributions of the GNS Science catalog of templates (dotted lines) and the final matched-filter catalog (solid lines) for 2012–2015. Northern and southern Ngatamariki (Nga N and Nga S) are shown in black and gray, respectively. The magnitude of completeness (M_c) and b value are calculated for the full matched-filter catalogs using the maximum curvature method (Wiemer & McNutt, 1997). Calculated values of M_c and b are noted in the top right.

seismicity may be triggered not by pore pressure perturbation, implying hydraulic connection to a wellbore, but by static and dynamic stress transfer onto suitably oriented fractures outside the reservoir (e.g., Cappa et al., 2019; Riffault et al., 2018). Numerical modeling of the temperature, pressure, and stress changes associated with injection will be required to better understand the effect of injection on fracture stability and the role of seismicity in increasing reservoir permeability (e.g., Ghassemi et al., 2007; Riffault et al., 2018).

4.3. Magnitude

We calculated magnitudes for 3,725 of the 41,114 located events using the methodology outlined in section 3.3. This large drop in the number of events is a result of the stringent correlation cutoff imposed (≥0.6 at four or more stations; see section 3.3), which ensures we retain only high-quality events. Figure 4 shows the frequency-magnitude distributions for both the GNS Science catalog (dotted lines), constituting the original template events, and the detected events for which we could calculate a local magnitude (solid lines). Here we show the catalog separated into northern and southern clusters. In both clusters, the additional matched-filter detections decrease the minimum magnitude in the catalog to less than zero.

We determine the b values for the matched-filter catalogs for a magnitude of completeness (M_c) calculated using the "maximum curvature" method (Wiemer & McNutt, 1997). However, we note that, due to the gradual roll-off of these distributions at lower magnitudes (especially for northern Ngatamariki), the maximum-curvature estimation method likely underestimates M_c (Wiemer, 2000). Notably, the inclusion of the matched-filter detections does not appreciably lower the magnitude of completeness of the catalogs here, in contrast to what has been shown elsewhere (e.g., Shelly et al., 2016). Interestingly, the original catalogs were not complete even at higher magnitudes, as suggested by the higher numbers of matched-filter detections for events above M_L 2.0 when compared to the GNS Science catalog.

We suggest that the difference in b value between the northern and southern clusters (1.84 and 1.20, respectively) reflects a difference in the sizes of fractures and faults that are hydraulically connected to nearby injection wells. The entire field is extensively fractured, as indicated by the available image logs of the injection wells (Halwa, 2013a, 2013b; Massiot et al., 2012), but in the south the active Aratiatia Fault Zone intersects injection wells NM06 and NM10 (Halwa, 2013b). The structures associated with this fault zone may be larger than those in the less permeable northern portion of the reservoir where active structures are harder to identify (Massiot et al., 2012), allowing for larger-magnitude events to nucleate. During injection operations elsewhere, higher b values (~1.5–2.0) have been observed nearer the injection point where high pore fluid pressures can induce slip on fractures subject to low differential stress (e.g., Bachmann et al., 2012). Slip on these less stressed fractures may be the explanation for higher b values at injection sites and volcanic regions (Wiemer et al., 1998). This may also affect the b values at Ngatamariki, where WHP in the northern injection zone is consistently ~0.5 MPa higher than in the south.

5. Analysis and Interpretation of Well Stimulation

Injection wells NM08, NM09, and NM10 underwent injection testing before the commissioning of the Ngatamariki power plant in 2013. These tests provide us the opportunity to study the seismic response to a number of isolated injections without contamination from concurrent injection from nearby wells. Below, we discuss each of these tests in detail and relate the characteristics of the accompanying seismicity to the injection parameters and geology in the respective part of the reservoir. Where possible, we calculate the well injectivity index, which we use as a proxy for near-well reservoir permeability (Watson, 2013). Typically, injectivity varies as t^n, where t is the time since the start of injection and n takes a value between 0.1 and 1.0 for most geothermal wells (Clearwater et al., 2015; Grant et al., 2013). For cold-water injection into high-temperature reservoirs, this injectivity increase is generally thought to reflect increased fracture aperture as the fracture walls contract (Grant et al., 2013).

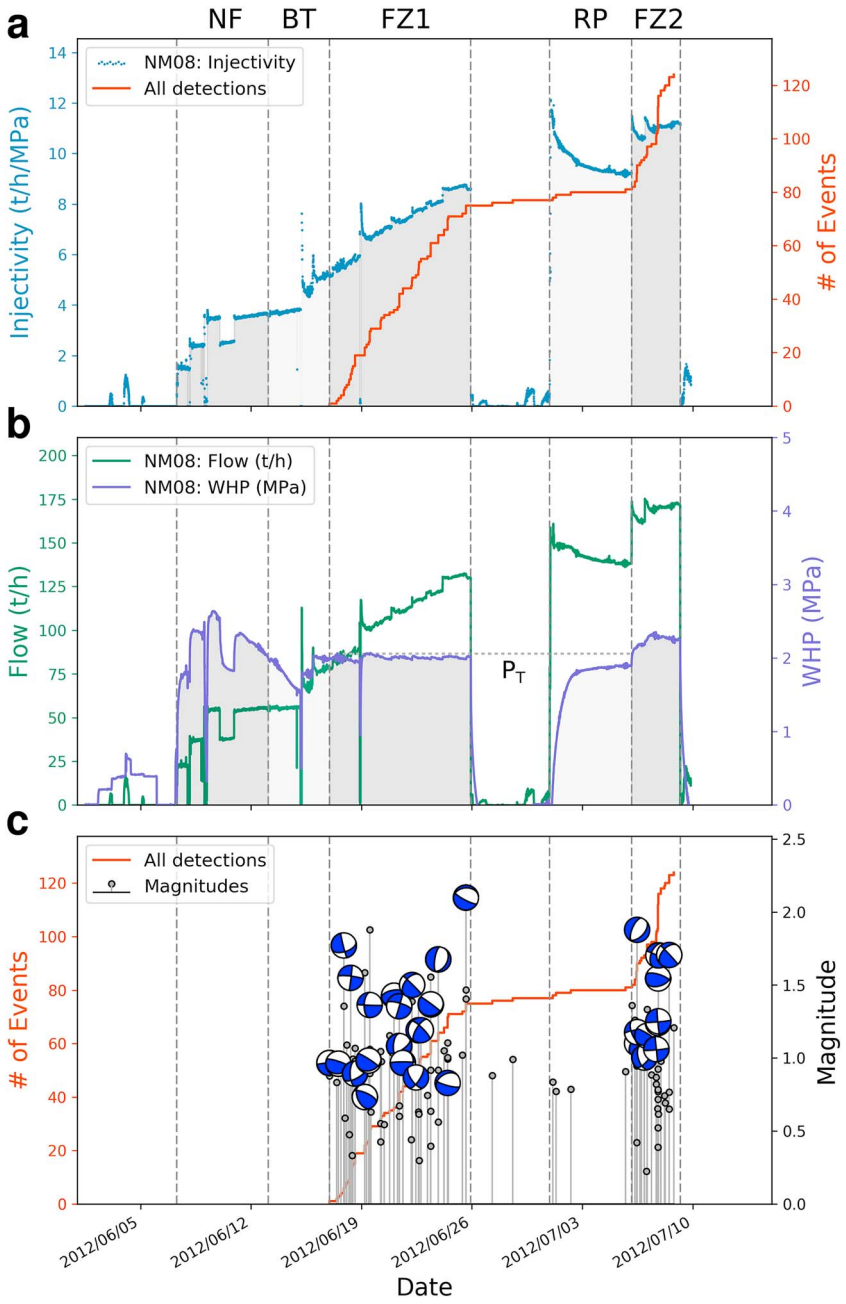

Figure 5. Summary of seismicity and injection parameters during the cold-water stimulation of NM08. (a) Cumulative seismicity versus injectivity index, (b) wellhead pressure versus flow rate, and (c) local magnitudes and available focal mechanisms solutions for the stimulation of NM08. Labels at the top of the plot delineate the following periods of interest: NF: near-field pressurization of the fracture zones surrounding the dike swarm, BT: breakthrough of pressurization from the near-well reservoir to the seismically active fracture zone, FZ1 and FZ2: fracture zone pressurization and associated seismicity, RP: renewed pressurization of the near-well reservoir. Once the fracture zone pore fluid pressure exceeds the maximum-induced pressure during FZ1 (P_T), seismicity is again induced. These periods are detailed in the schematic in Figure 6. WHP = wellhead pressure.

5.1. Northern Injection Zone

5.1.1. NM08 Stimulation

Starting on 8 June 2012, NM08 underwent a cold-water stimulation treatment, accepting ~66,000 m^3 of water over a period of approximately 1 month. This was the first injection test in the field, and it triggered a sharp increase in the rate of microseismicity, which occurred predominantly in one cluster at the depth of the well's main permeable zone at ~2,000 m bsl (Figures 5 and 7). A plane fit to the hypocenters of this

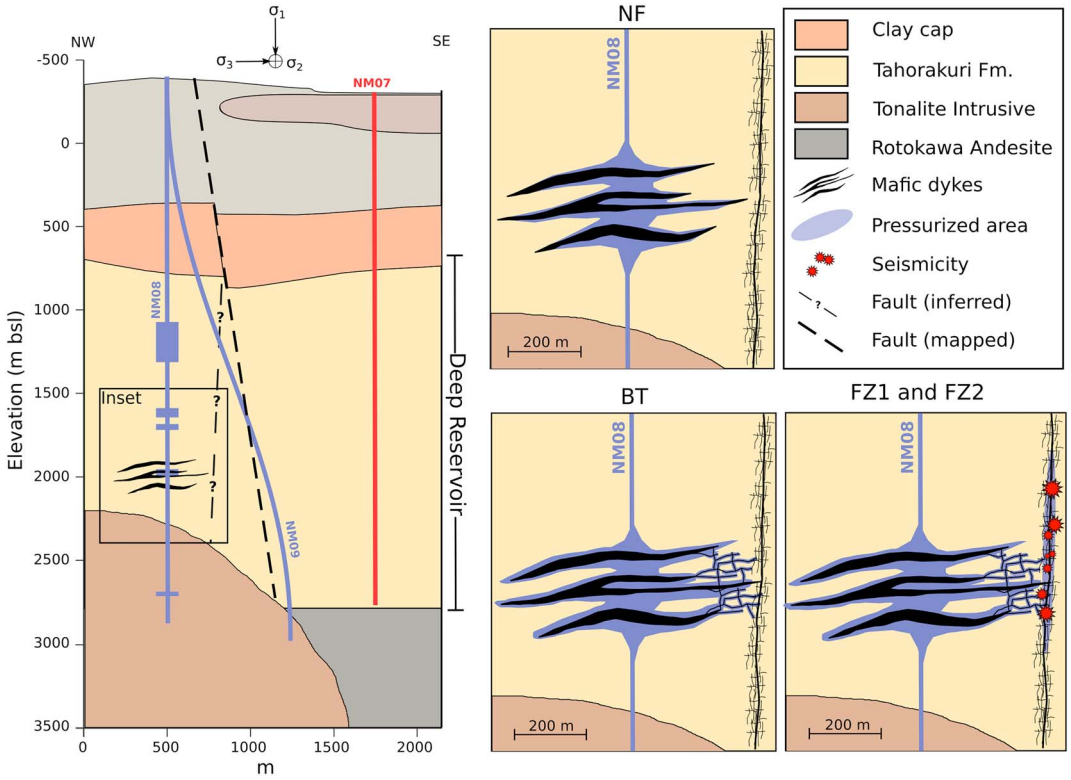

Figure 6. Schematic illustrating the sequence of events occurring at depth during NM08 stimulation. The headings of the inset panels correspond to the periods labeled at the top of Figure 5, and NM08 feed zones are indicated by rectangles overlain on the well. The main permeable zone in well NM08 corresponds to a depth where the well intersects a mafic dike swarm. During NF, hydraulic conductivity between NM08 and the soon-to-be-active fracture zone was low. This period corresponds to a pressurization of the small, near-well fracture network hosted in and around a set of mafic dikes, hence the relatively high wellhead pressure (WHP) but lack of seismicity. During BT, while WHP was below 2 MPa, a hydraulic connection was established with the fracture zone, consistent with increasing injectivity at the well. During FZ1, once WHP was increased to a steady 2 MPa, the pressure perturbation was able to diffuse into the fracture zone, weaken suitably oriented fractures, and generate seismicity. At the start of phase two, the fracture network repressurized until it reached the maximum pressure encountered during phase one, at which point seismicity recommenced (FZ2). NF = near field; BT = breakthrough; FZ = fracture zone.

cluster strikes ~192°and dips ~66° to the NW, centered on a depth of roughly 2,000 m bsl. This is consistent with measurements of fracture orientation made from image logs, which suggest a dominant NE-SW strike for fractures intersecting the well and a dominant NW dip over this depth interval (Massiot et al., 2012). Flow rate, WHP, and injectivity index are shown in Figure 5.

Figure 5 shows the cumulative number of microseismic events during the NM08 stimulation, which included two phases of injection. The first, starting on 8 June 2012 did not immediately trigger an increase in the rate of seismicity. Instead, there was a period of approximately 10 days during which there were no detected events. We interpret this period to correspond to near-field (NF) pressurization of the reservoir followed by pressure breakthrough (BT) to a highly permeable fracture zone (Figures 5 and 6). This period of testing involved a step rate injection test in which the WHP response was observed for incremental changes in flow rate. Following this period, on 15 June (middle of BT; Figure 5) the injection was changed from a steady flow to a steady pressure regime in which flow rate was allowed to vary. This change also corresponded to a modest increase in both the injection rate and WHP. Roughly 2 days after this change, the rate of seismicity increased to between 5 and 12 events/day in the area of NM08 and this increased rate was maintained until the first phase of injection ended on 26 June (FZ1; Figure 5), accompanied by an abrupt halt to seismicity.

Phase two of the stimulation began on 1 July 2012 (start of renewed pressurization; Figure 5) at slightly higher flow rates than previously (~150 t/hr). Again, the rate of seismicity did not immediately increase once the second phase of injection began. There was a delay of approximately 4 days before the flow rate was

increased to ~175 t/hr with an accompanying increase in WHP of approximately 0.5 MPa (FZ2; Figure 5). Following this increase, the rate of seismicity increased to 23 events per day (T5), slightly higher than the levels encountered during phase one. This activity ceased as soon as injection was halted on 9 July, bringing the total number of events during the stimulation to 122. The maximum M_L during the entire stimulation was 2.1.

Assuming that NM08 is hydraulically connected to a set of fractures, we expect seismicity to occur once an induced pressure front has reached a critically stressed subset of fractures in the local stress regime. The advance of the induced pressure front is controlled by the hydraulic diffusivity of the reservoir (also referred to as transmissivity, the permeability thickness product: kh), which is closely linked to the reservoir permeability. This relationship has led other groups to develop seismicity-based reservoir characterization (SBRC) to infer diffusivity from the location and occurrence time of induced seismicity (e.g., Jeanne et al., 2015; Parotidis et al., 2004; Shapiro & Dinske, 2009; Shapiro et al., 2002). At Ngatamariki, and at most other naturally fractured reservoirs, flow is strongly influenced by the spacing and permeability of fractures (Grant & Bixley, 2011). If we consider a large enough volume of the reservoir, relative to the fracture spacing, SBRC can be useful in estimating a bulk reservoir diffusivity from the occurrence of seismic events. However, if flow is concentrated in a small number of highly permeable fracture zones (highly anisotropic permeability), as is the case at Ngatamariki, SBRC is less useful in describing reservoir properties. In addition, SBRC assumes that events are triggered purely by injection-related pore fluid pressure perturbation. However, a variety of mechanisms are responsible for triggering seismicity, many of which are unrelated to the hydraulic properties of the reservoir, leading to speculation as to the utility of SBRC (Cappa et al., 2019; Riffault et al., 2018). Nevertheless, we have fit a number of curves to the seismicity for each of the injection scenarios detailed in this work (Figure S5).

The timing and location of seismicity during the stimulation of NM08 provoke a number of questions:

1. Why does seismicity lag behind the start of injection by up to 10 days?
2. Conversely, why does seismicity stop immediately following a halt of injection?
3. Why are the increase in injectivity index and seismicity poorly correlated in time?

Seismicity trails injection by 10 days at the outset of the stimulation and again by 4 days at the start of phase two (NF and renewed pressurization; Figure 5). In the first tens of minutes following the start of injection, drilling-related degradation of near-well permeability (i.e., positive skin effects; Grant & Bixley, 2011) may have contributed to a delayed pressure response between the well and reservoir. However, as the seismic lag time was of the order of days, positive skin effects (normally of the order of hours) cannot account for this observation (Horne, 1995). The outward advance of the pressure front may also have been slowed by compression of the fluid-solid reservoir system. However, the Ngatamariki reservoir is slightly overpressured at depth and the measured pressure drawdown more than 1 year after the stimulation of NM08 was <0.2 MPa (Quinao et al., 2017). A small zone of boiling is known to exist roughly 500 m south of NM08 at a depth of 500 m bsl (Quinao et al., 2017). Although we have not quantified the possible significance of this zone, for fluid compressibility to explain the 10-day lag from the start of injection to the onset of seismicity, this steam would need to be present at NM08 feed zone depths (>1500 m bsl), for which there is no evidence.

The main permeable zone of NM08, which coincides with the depth of seismicity during stimulation, is defined by a series of mafic dikes or sills (Chambefort et al., 2014; Massiot et al., 2012; Figure 6). Image log quality at this depth is poor, and the orientation of these dikes is poorly constrained (Massiot et al., 2012), but their emplacement orientation is likely to have been controlled by the prevailing stress field 0.64–0.79 Ma (Chambefort et al., 2014) and related to the emplacement of the tonalite intrusive at the bottom of the well (Figure 6). If we assume that flow is concentrated within the damage zone surrounding the dikes and/or within the dikes' internal structures (such as cooling joints or flow bands; Massiot et al., 2017), it may be that these structures are not optimally oriented for failure in the current stress regime. Although the prevailing tectonic environment during emplacement of the intrusive was similar to that of the present (i.e., active rifting; Wilson & Rowland, 2016), highly active volcanism in the TVZ, including the subsequent formation of the adjacent Whakamaru caldera (0.35 Ma), would likely have modified the Ngatamariki stress state (Wilson et al., 1995).

We hypothesize that initial flow from NM08 was concentrated in these noncritically stressed dike-related structures and therefore did not trigger detectable seismicity (NF; Figures 5 and 6). In this case, the time

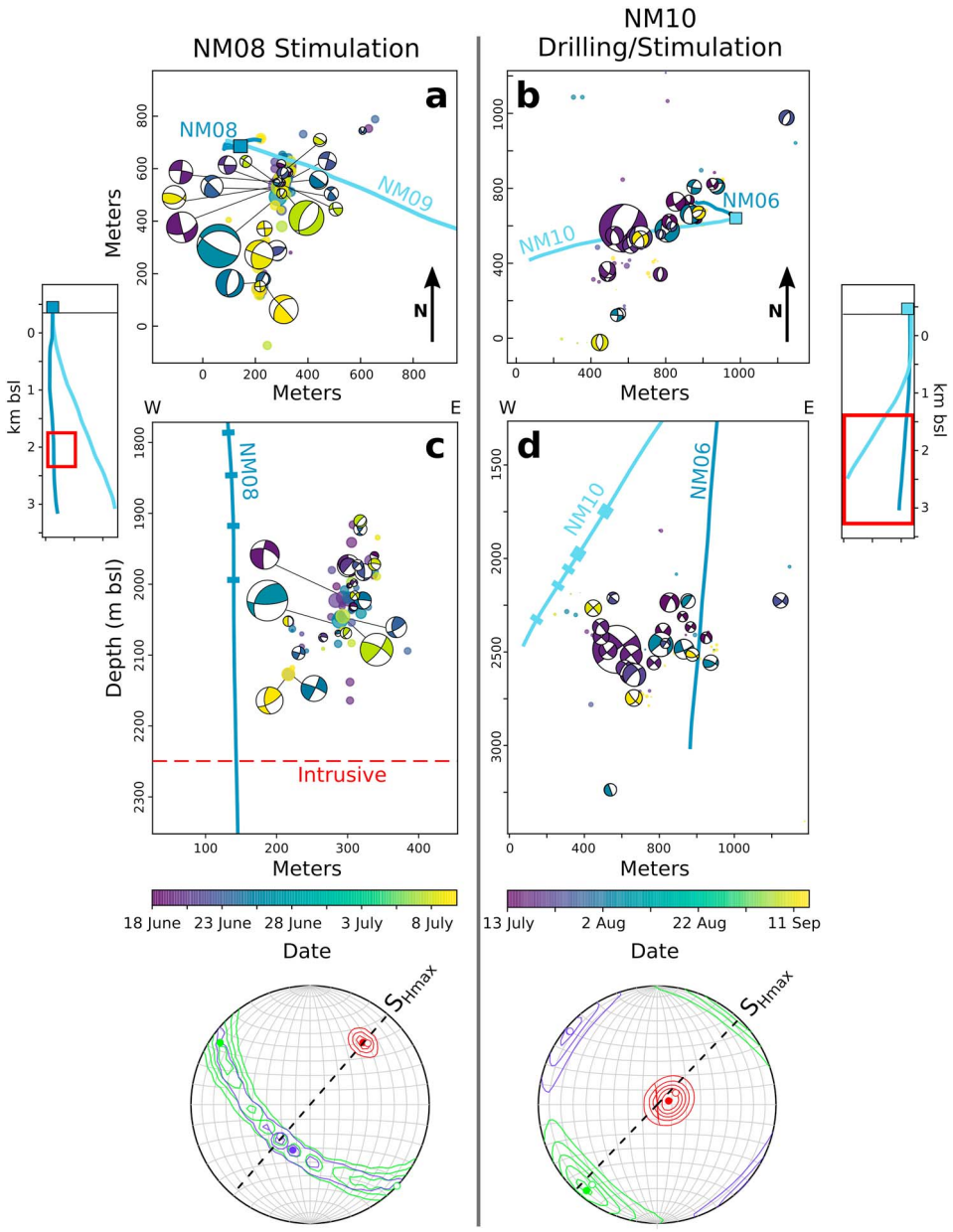

Figure 7. Hypocenters and *P* wave, first motion derived focal mechanisms (where available) for events that occurred prior to startup of the Ngatamariki plant. Where offset from the actual location, mechanisms are connected to their hypocenter with a line. (a, b) Map views with the wellhead shown as a blue box and the surface projection of the boreholes shown as blue lines. (c, d) Cross sections whose extents are indicated in the small inset to either side of the figure. The rectangles overlain on the boreholes in cross section indicate the inferred feed zones for each well. Mechanisms in panels (a) and (c) occurred during stimulation of NM08, in the northern injection zone, while mechanisms in panels (b) and (d) occurred during NM10 drilling losses and injection testing in the southern injection zone. All symbols are colored by their date of occurrence and the symbols plotted in cross sections (c) and (d) have been reprojected to reflect the different viewpoint (from the south). The stereonets at the bottom of the figure show stress inversion results (lower hemisphere) from the focal mechanisms presented in panels (a) and (c) (left stereonet) and panels (b) and (d) (right stereonet), with red contours representing the probability density of the direction of σ_1, green representing σ_2 and blue representing σ_3. The black dashed line indicates the direction of S_{Hmax}. In panel (c), the red dashed line indicates the top of the intrusive sequence in northern Ngatamariki.

lag in seismicity corresponds to a period of NF pressurization during which NM08 was not hydraulically connected to the fracture zone defined by the hypocenters in Figure 7 (striking 192°, dipping 66°NW, as defined by a least squares fitting of a plane to the hypocenters). If we consider an alternative scenario, in which NM08 was always hydraulically connected to the fracture zone, then we would expect seismicity to have been triggered by the diffusion of the maximum observed WHP to the fracture zone (2.6 MPa during NF; Figure 5). However, this scenario is unlikely in view of the immediate shutoff of seismicity when the well was shut-in, which would imply hydraulic diffusivities an order of magnitude greater than those required by diffusion of the maximum WHP to the fracture zone. It may also be the case that undetected seismic (or entirely aseismic) slip/opening near the wellbore transferred stress onto a remote, hydraulically isolated fracture zone, triggering failure (e.g., Cappa et al., 2019; Rinaldi & Rutqvist, 2019). We discuss this possibility in more detail at the end of this section.

We infer that, during the NF phase, a small set of NF fractures was pressurized, with a maximum measured WHP of 2.6 MPa (the highest WHP measured at Ngatamariki to date). Seismicity was induced in the fracture zone (roughly 200 m from NM08) during a period of constant 2.0-MPa WHP (FZ1; Figure 5). The hydraulic connection to the fracture zone would need to have been established while the WHP was below this ~2.0-MPa threshold, otherwise seismicity would have been induced earlier. The degree to which the fracture zone was critically stressed may also explain a part of the time lag during what we call "BT" (Figure 5), as it may have taken time for the pressure perturbation to reach the value, ΔP_{crit}, at which it induced slip.

A common observation during injection operations worldwide is postinjection, persistent seismicity (e.g., Fehler et al., 1998; Rutledge & Phillips, 2003; Shapiro et al., 2002). Many of the largest injection-induced events have occurred after shut-in of the injection wells in question (e.g., Mukuhira et al., 2017, at Basel). At Ngatamariki this was not the case, as near-well seismicity ceased with the halt in injection for both phases of the NM08 stimulation (end of FZ1 and FZ2; Figure 5). Assuming an unbounded reservoir, the relaxation of the shut-in-induced pressure perturbation is also a diffusive process (termed the "back-front" of seismicity by Parotidis et al., 2004). In the NM08 case, an immediate cessation of seismicity on shut-in would imply nearly infinite reservoir permeability between the well and the seismically active zone. This is incompatible with flow through the reservoir rock matrix, which has a calculated in situ permeability of 6×10^{-18} m^2 (Cant et al., 2018) but could occur if the effective reservoir permeability is controlled by fractures. If we conceptualize the set of fractures connecting NM08 to the active fracture zone as a series of pipes with effectively infinite permeability, then a pressure perturbation applied at one end produces a near-instant pressure response on scales hundreds of meters (the so called "water hammer" effect; Ghidaoui et al., 2005). The fracture network at Ngatamariki would have sufficient permeability to transmit these pressure perturbations rapidly to distances hundreds of meters, far enough to reach the seismically active zone. Once a drop in pore fluid pressure has propagated to the critically stressed fracture zone (~200 m from NM08), seismicity should cease. We suggest that in order for the initial time lag and eventual rapid halt in seismicity during NM08 stimulation to coexist, the hydraulic conductivity between NM08 and the seismically active fracture zone must have been established during the injection (during BT; Figure 5).

Injectivity gain and seismic slip during the stimulation of NM08 are not well correlated. During phase one of injection (NF, BT, and FZ1), injectivity increased significantly ($n = 0.6$–0.7, where injectivity increases as t^n for geothermal wells; Clearwater et al., 2015; Grant et al., 2013), indicating that near-well permeability was increasing. However, during NF pressurization, no seismicity was detected, suggesting that the initial permeability enhancement resulted from aseismic processes as has been observed elsewhere (Cornet, 2016, and references therein). Seismicity and injectivity increased simultaneously throughout FZ1 (Figure 5), but the rate if injectivity increase had already been established prior to the onset of seismic slip (BT; Figure 5).

The exact nature of the aseismic displacements responsible for the observed permeability increase is difficult to characterize. A number of recent works have shown that a similar increase can be modeled by both aseismic hydroshear (i.e., through self-propping of preexisting fractures; Rinaldi & Rutqvist, 2019) and fracture normal displacement (Guglielmi et al., 2015). While Rinaldi and Rutqvist (2019) were able to adequately model pressure evolution during a series of Fenton Hill Hot Dry Rock injections for the case of either elastic opening or pure shear on a single fracture zone, the hydroshearing model better recreated the observed flowback during postinjection venting. For the Guglielmi et al. (2015) case of targeted injection into a decameter-scale fracture, fracture normal displacement, as opposed to shear movement, was shown

to account for most of the estimated permeability increase. It should be noted that the scale, temperature, and depth of the Fenton Hill site more closely resemble the Ngatamariki reservoir than does the LSBB laboratory in France studied by Guglielmi et al. (2015). Rinaldi and Rutqvist (2019) also explicitly account for thermoelastic effects of injection into a hot reservoir, which may play a large role in influencing the effective stress state of a fracture zone targeted by injection (e.g., Ghassemi et al., 2007). These effects cannot be replicated at the temperature of the in situ experiments of Guglielmi et al. (2015). Unfortunately, while a number of potential mechanisms of permeability increase can explain the observations shown here, we cannot determine the sense of displacement on the fracture zones at NM08, only that these displacements were likely aseismic.

As mentioned above, the large temperature contrast between injected fluid and reservoir rock at Ngatamariki (up to ~226 °C) likely influenced the effective stress on the near-well fracture network as a result of thermal contraction of the fracture walls (e.g., Ghassemi et al., 2007). As suggested by Stephens and Voight (1983), the thermally induced circumferential stress at the wellbore is (Zoback, 2010)

$$\Delta\sigma_T = -\frac{\alpha_L E \Delta T}{1-\nu} \tag{6}$$

with α_L being the coefficient of thermal expansion of reservoir rock, E the Young modulus, ΔT the temperature difference between reservoir rock and injectate, and ν Poissons ratio. We assume $\alpha_L = 1 \times 10^{-5}\mathrm{K}^{-1}$ (Bauer & Handin, 1983), $E = 20 \times 10^9$Pa (Cant et al., 2018), $\nu = 0.25$, and a temperature difference of 204 °C (interpreted from pressure-temperature spinner data at feed zone depth during stimulation). This yields a thermal stress at the wellbore of approximately −54 MPa. In the future, numerical modeling of the thermoporoelastic problem should be undertaken in order to characterize the effect of thermal contraction on the stability of the fracture network and to determine the utility of using hypocentral locations to estimate the extent of the permeable reservoir (e.g., Ghassemi et al., 2007; Riffault et al., 2018). However, the lack of seismicity suggests that such cooling effects may have stabilized the fracture network, consistent with preferential reduction of σ_1 ($\approx \sigma_V$) due to density-driven, downward flow of the cold injectate (as detailed by Jeanne et al., 2015).

The thermal diffusivity of the reservoir matrix is typically orders of magnitude lower than the effective hydraulic diffusivity of the reservoir (mm^2/s and m^2/s, respectively; Kanamori et al., 1968; Shapiro et al., 2006). Nevertheless, these thermal effects likely dominate the increase in well permeability at NM08. This model of thermal expansion-driven stimulation has been proposed by Grant et al. (2013) and Siega et al. (2014), who tested it against a number of geothermal injectivity data sets in New Zealand and elsewhere. Self-propping of slipping fractures, which is associated with seismic slip, is also known to increase fracture permeability (e.g., Lee & Cho, 2002), and this process undoubtedly influences the permeability of the seismically active fracture zone. However, the injectivity increase as measured at the well appears to be far more sensitive to other, aseismic processes, which we suggest is dominated by near-well thermal contraction of the fracture network walls.

Phase two of NM08 stimulation was also accompanied by a time lag (this time of four days) prior to the response of seismicity. In this case, the lag corresponds to the time needed to exceed the previous highest pore pressure perturbation (P_T; Figure 5). Assuming that hydraulic connectivity from NM08 to the active fracture zone was not established until the BT period (Figures 5 and 6), the highest pressure perturbation to which the fracture zone was subjected during the period of seismic slip corresponded to a WHP of roughly 2 MPa. As soon as WHP exceeded this 2-MPa threshold during phase two, seismicity restarted. This reinforces the interpretation of a high-permeability fracture network within 200 m of NM08 following the NF and BT periods of phase one (Figure 5).

Recent research by Cappa et al. (2019) shows that fluid injection can encourage rate-strengthening behavior of a fracture, implying that seismic slip, even on a targeted fracture or fault, is triggered by poroelastic stress transfer away from the pressurized zone due to aseismic, near-well displacement. Therefore, an alternative explanation for the triggering of seismicity at NM08 never requires a hydraulic connection between the well and the seismically active zone. Instead, seismic slip may have been purely the product of Coulomb stress transfer onto the active fracture zone by aseismic displacements near the wellbore. As described above, near-wellbore aseismic displacements were likely induced by a combination of thermoelastic contraction of the rock matrix and pore-pressure increase in the feed zones.

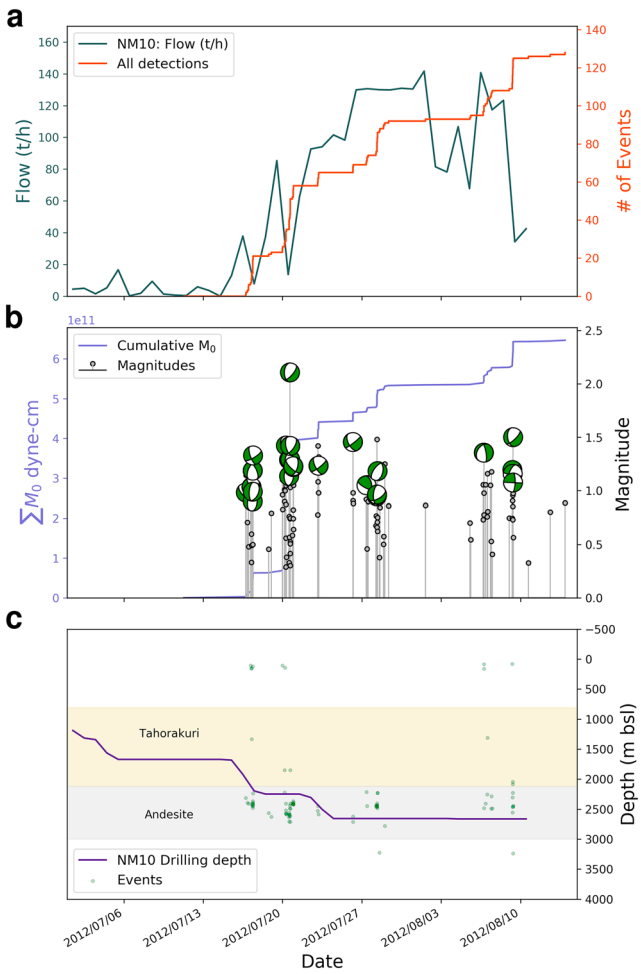

Figure 8. (a) Flow (t/h) during drilling losses at NM10 and cumulative seismicity versus time, (b) cumulative seismic moment with event local magnitudes and available focal mechanisms during drilling of NM10, and (c) drilling depth with depth of seismic events. The two main geological units within the southern reservoir, the Tahorakuri Volcaniclastics and Rotokawa Andesite, are depicted in (c) for context.

5.1.2. NM09 Injection Testing

Injection well NM09, in the north of the field, underwent two periods of injection prior to plant startup (Figure S4), accepting roughly 60,000 m^3 of fluid for each. Only 11 seismic events were detected within the reservoir during both phases of NM09 stimulation combined, likely due to the well's high-permeability feed zones that inhibited pressure buildup in the reservoir during injection (WHP <0.1 MPa; Figure S4). Despite the lack of seismic slip, injectivity increased during the tests (n =~0.4–0.6; Clearwater et al., 2015). As at NM08, this observation indicates that permeability was enhanced through undetected (small) seismic slip, aseismic slip/opening of permeable zones connected to the wellbore, or both. It also reveals an even stronger decoupling of injectivity increase and near-well seismicity than at NM08, with the observed gain likely a result of thermoelastic stresses near the wellbore, especially during cold-water injection in phase one.

5.2. Southern Injection Zone

5.2.1. NM10 Drilling Losses and Injection Testing

Well NM06 was drilled and tested in the southern injection zone many years prior to our study. As a result, drilling and well testing in southern Ngatamariki during this study period was limited to injection well NM10. Injection began once drilling had reached the depth of the deep (andesite) reservoir and drilling fluid losses occurred (at depths >2000 m bsl). This was followed by a formal injection/stimulation test once drilling had been completed. The microseismic response to the drilling losses was larger than the response during the actual injection test (Figures 8 and 9). At the end of drilling, approximately 57,000 m^3 of drilling fluid (largely water) had been lost to the formation, a comparable volume to that in the other injection

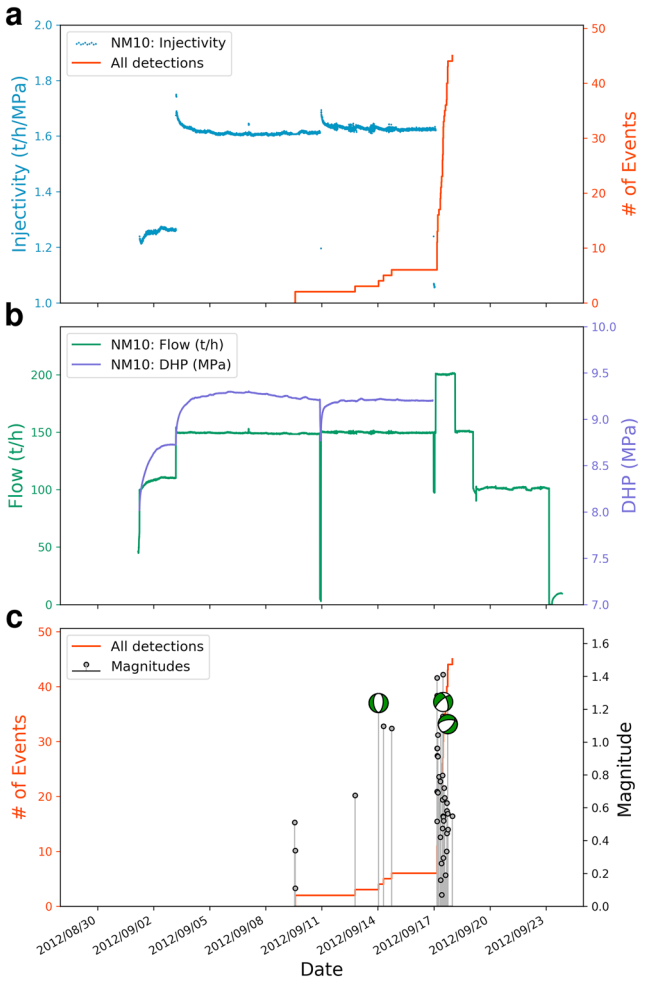

Figure 9. (a) NM10 injection test II versus cumulative seismicity in southern Ngatamariki, (b) flow rate and downhole pressure. DHP ends on 17 September as the measurement tubing was traversed to a greater depth (from 1,228 to 2,050 m). (c) Cumulative seismicity in red with the magnitude and available focal mechanism solutions as stems. DHP = downhole pressure.

tests analyzed and described above. Data on fluid flow during drilling are sampled less frequently than the flow rate during injection tests, but daily records of drilling losses correlate well with seismicity in southern Ngatamariki as shown in Figure 8a. NM10 drilling reached 1,700 m bsl on 6 July 2012, and significant fluid losses were incurred from 13 July (~2,100 m bsl).

Seismicity began as the drilling reached the depth of a major fault zone identified in the NM10 image logs (there are six identified faults between 2,100 and 2,300 m bsl, within the Rotokawa Andesite; Halwa, 2013b) and continued for the remainder of the drilling (Figure 8c). These SE dipping structures, visible in image logs (Halwa, 2013b), are likely associated with the NE-SW striking Aratiatia Fault Zone (Figures 1, 3, and 7). Seismicity increased in short, 1- to 2-day-long bursts with the majority of events occurring after fluid losses had exceeded 25 t/hr. The lag between the start of fluid losses and the seismicity induced during NM10 drilling is roughly 3 days, 3 times shorter than at NM08. This lag may simply be due to the time needed to pressurize the fault zones, which dominate flow from NM10. However, aseismic opening of the fault zones via pore pressure increase and thermal contraction of the fracture walls, as observed by Guglielmi et al. (2015), may also have played a part. We would expect these processes to be accompanied by a corresponding increase in injectivity, but there are no pressure data during the drilling to confirm this. The seismicity occurred >700 m deeper than the main feed zones in NM10 (Figure 3) and closer to injection well NM06, which was shut-in during this period. This may indicate that fluid flowed down-dip along the fault zone to critically stressed points away from the well. The maximum magnitude during drilling at NM10 was 2.1, comparable to the stimulation at NM08 for a similar injected volume. This may indicate that the pressurized zones during NM08 stimulation and NM10 drilling were similar in volume, thereby affecting fractures and faults of similar size. However, as southern Ngatamariki exhibits a lower *b* value than in the north when the entire 4-year catalog is taken into account, we suggest that much larger structures exist in the south than in the north, which were only activated once high-volume injection began in 2013. As at NM08, seismicity ceased after end of drilling implying that the permeability of the fracture zone is considerable.

There were no drilling or injection activities in southern Ngatamariki between the drilling of NM10 and the planned injection test that occurred on 1–23 September 2012. There was also no detected seismicity during this period. Roughly 73,000 m^3 of fluid was injected during the test at flow rates of between 100 and 200 t/hr and downhole pressures of 7.5–9.4 MPa (Figure 9). As mentioned above, the unintended losses that occurred during drilling are considered the start of injection in southern Ngatamariki. Therefore, during drilling, NM10 may have undergone much of the increase in injectivity that otherwise would have occurred during the later injection test. It is possible that slip during drilling relieved most of the accumulated stress on the most critically stressed portions of the fault zone, making failure on these patches less likely during the injection test. This view is supported by the relative lack of seismicity during most of the test (Figure 9). Seismicity, while not absent, occurred for the first 2 weeks of the test at a rate of roughly one event per day and injectivity increased only slightly after the first step rate change in flow from ~100 to 150 t/hr. However, the rate of seismicity jumped dramatically (with nearly 40 events on 17 September alone) once injection was increased from ~150 to ~200 t/hr. We do not know the corresponding increase in downhole pressure for this step rate change because the pressure monitoring tubing was repositioned at that time. However, because the flow rate of 200 t/hr is significantly higher than was measured during either drilling or testing prior to this time, we can reasonably assume that permeability had increased during drilling losses and that an elevated flow rate would have been required to reach a critical pressure/stress to retrigger seismicity. The resulting increase in the rate of seismicity occurred

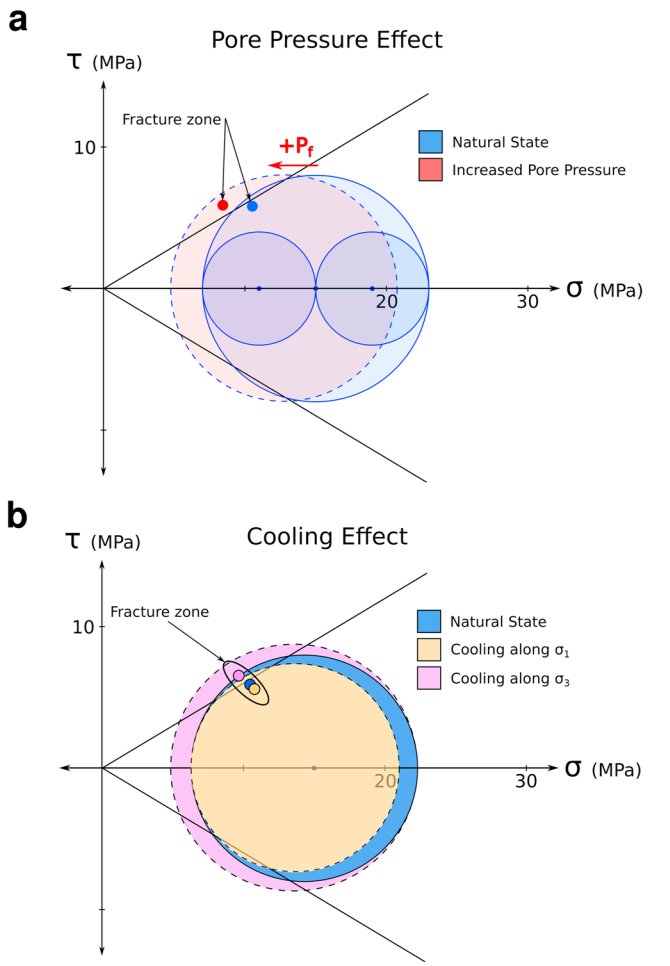

Figure 10. Schematic Mohr circles calculated for a depth of 2,000 m bsl illustrating the effect of (a) pore pressure increase and (b) thermal cooling of the fracture zone near-well NM08 (strike: 191°, dip: 66°). The natural state magnitude for σ_1 was determined by integrating density over depth using density values from well cuttings and core taken from NM08 (~45 MPa at 2,000 ms). The magnitude of σ_3 was extrapolated from leak-off tests conducted in Rotokawa (~29 MPa Davidson et al., 2012). Reservoir pressure is approximately 22 MPa at 2,000 m bsl. The failure envelopes represent cohesionless, preexisiting fractures with a coefficient of friction of 0.6. Circles in the figure represent the position of the plane defined by the hypocenters of seismicity during NM08 stimulation within each stress field. Plots are adapted from the output of *MohrPlotter* (Allmendinger et al., 2011).

within 2 hr of the increase in flow rate and at event-feed zone distances of up to 800 m (Figures 9a and 9b). As during FZ2 at NM08, inducing events at such distances so rapidly requires that pressure change be concentrated along a small number of highly permeable fracture zones, which is what we expect in NM10 on the basis of image logs. Once flow rate had subsided to below 200 t/hr, seismicity ceased, suggesting rapid progression of the back-front to the seismically active zone as was observed at NM08. The maximum magnitude during the injection testing of NM10 was 1.4, lower than during NM10 drilling, possibly as a result of the stress acting on the fracture zone having been relieved during drilling fluid losses.

5.3. Focal Mechanisms and Stress

Figure 7 shows the focal mechanisms calculated for microearthquakes that occurred during the three injection tests described above and the corresponding stress inversion results for northern and southern Ngatamariki prior to plant startup. The events that occurred during drilling and injection testing of NM10 (Figures 7b and 7d) delineate a structure associated with the Aratiatia Fault Zone, as mentioned above. The majority of the 28 focal mechanisms we calculated for southern Ngatamariki during this time period show predominantly normal faulting, with most fault planes striking N-S or NE-SW. This result agrees well with what is known about the extensional regional stress regime and the local faults in the central TVZ, which are typically oriented NE-SW (Massiot et al., 2015). Acoustic- and resistivity-based image logs for NM10 confirm this preferred NE-SW fracture orientation at reservoir depths with predominantly SE dips (Halwa, 2013b). As mentioned in sections 1.3 and 4.2, rapid injection returns during a tracer test conducted in January 2014 also indicate that a highly permeable flow pathway connects NM10 to production well NM05 (Buscarlet et al., 2015). The locations of the events induced during NM10 drilling and injection testing are likely related to fluid flow along this structure.

Stress inversion results for southern Ngatamariki (Figure 7) show σ_1 to be subvertical and the direction of maximum horizontal compressive stress (S_{Hmax}) to be NE-SW, consistent with previous findings for the central TVZ (Townend et al., 2012) as well as measurements of borehole breakout in NM10 which indicate an S_{Hmax} azimuth of 210° (Halwa, 2013b). This result is also consistent with borehole tensile failure measurements from the Rotokawa geothermal field, 5 km to the south (McNamara et al., 2015).

The 58 mechanisms in Figures 7a and 7c correspond to events that occurred during the stimulation of NM08 and exhibit a greater variety of faulting kinematics than in the south. Many of these mechanisms show primarily reverse or oblique strike-slip movement with at least one nodal plane striking NW-SE, which agrees with the orientation of the plane defined by the hypocenters of the events (strike 192°, dip ~66°). The remaining mechanisms show normal faulting with a variety of strikes. The occurrence of compressional faulting is rare within the central TVZ and may be related to stress field rotation during the emplacement of the intrusive body and mafic dikes.

Stress inversion results for northern Ngatamariki differ from those in the south (Figure 7). While the direction of S_{Hmax} is unchanged throughout the reservoir (NE-SW), σ_1 is dipping NE at approximately 30° in the north and σ_2 and σ_3 define a girdle. It is possible that the stress state in this section of the reservoir was already rotated into an orientation suitable for reverse faulting by the emplacement of the tonalite intrusive body and dikes. Massiot et al. (2012) showed that the in situ horizontal stress field rotates counterclockwise by 28° near the contact between the Tahorakuri and the intrusive body (below the main permeable zone and dikes, relative to the stress field above), which may indicate an intrusive-related effect on the stress state.

What is not known is the effect of injection-related pressure buildup and thermoelastic stresses on the stress in the reservoir (Figure 10). We have no DHP measurements during stimulation of NM08. However, WHP reached 2.6 MPa during the NF period of stimulation (NF; Figure 5). Figure 10a shows the destabilizing effect of pore pressure increase on the reservoir stress state, with the increase in P_f exaggerated for visibility. We infer that the fracture zone defined by the seismicity during NM08 stimulation is nearly critically stressed within the reservoir stress regime and would require only small increases in pore pressure to induce slip (blue and red circles; Figure 10a).

Circumferential stresses reached roughly −54 MPa at the wellbore (at 2,000 m bsl), but it is difficult to determine how far such thermoelastic effects would propagate from the well as the propagation of the thermal front is dependent upon the flow pathways and flow rate through the reservoir. During a stimulation operation at the naturally fractured Geysers geothermal field, Jeanne et al. (2015) modeled a similar thermal front propagating >100 m in the span of 2 months. For a reservoir where fluid flow is fracture dominated, the corresponding cooling effect depends on the predominant direction of flow relative to the principle stress axes, as illustrated in Figure 10b (Jeanne et al., 2015). This is because the rock matrix is cooled conductively only within <1 m along the normal to a fracture plane, whereas it is cooled for many tens of meters along the strike of a fracture, leading to an anisotropic volume of thermal cooling (Simone et al., 2013; Jeanne et al., 2015). Initial, gravity-driven (downward) flow of cool fluid at NM08 would preferentially decrease σ_1 and stabilize the near-well fracture network (yellow Mohr circle; Figure 10b). This may have contributed to the lack of seismicity during the NF and BT periods of NM08 stimulation (Figures 5 and 6). As fluid begins to spread laterally from the well, the cooling effect preferentially lowers the horizontal stress that is best aligned with the direction of flow. At Ngatamariki, fluid flow parallel to σ_3 (NW-SE) would act to destabilize the fracture network (pink Mohr circle; Figure 10b), including the structure along which seismicity occurred, which is represented as a colored circle for the various stress fields illustrated in Figure 10.

As the Ngatamariki reservoir is structurally similar to that of the Geysers, in that they are both naturally fractured, high-temperature fields, it is possible that a thermoelastic front could have reached the location of seismicity during stimulation of NM08 and therefore influenced the stress state in the fracture zone. Also at the Geysers, Martínez-Garzón et al. (2013) observed temporal changes in focal mechanism-derived stress tensors related to various fluid injection operations including the injection operation modeled by Jeanne et al. (2015), although this contrasts with the findings of Boyle and Zoback (2014) who found that operations at the Geysers had little effect on the reservoir stress state. We cannot rule out the possibility that the deviation of the stress field from the regional trend in northern Ngatamariki is injection related, although we think it unlikely. As discussed above, it is more likely that the stress state was already rotated in the northern injection zone prior to injection.

6. Conclusions

Ngatamariki constitutes an important case study of isolated injection into a little-modified reservoir. In this paper we present a nearly 4-year catalog of microearthquakes at the Ngatamariki geothermal field spanning periods of initial field development, well drilling, and plant startup. Individual tests at each well were isolated from one another in both time and space, which has allowed us to observe the response of microseismicity to injection at individual wells. Seismicity occurs in two spatial clusters centered on the northern and southern injection zones. In the north, stimulation of well NM08 induced more than 120 events in 1 month, while injection testing of nearby well NM09 generated only 11 events in nearly 3 months. In southern Ngatamariki, drilling and injection testing of NM10 generated nearly 200 events over an interval of roughly 3 months. The difference between the frequency-magnitude distributions of the northern and southern clusters provides a clear example of b value dependence on the characteristics of the local fracture network. In the north, the fractures that are hydraulically connected to wells NM08 and NM09 are smaller than those in the south, where fluid is injected into a large, active fault zone. As a result, larger events are able to nucleate in the southern injection zone ($b = 1.20$) than in the north ($b = 1.84$), resulting in a lower b value.

Focal mechanisms calculated for events that occurred during these injections show different faulting regimes in the northern and southern halves of Ngatamariki. During the stimulation of NM08, in the northern part of the field, focal mechanisms exhibited a wide range of faulting kinematics, most with at least one nodal plane consistent with the NNE-SSW trend in hypocenter locations and a stress state with σ_1

dipping 30°. In contrast, NE-SW striking normal faulting mechanisms make up the bulk of events occurring in the south. We interpret this contrast to be related to the presence of the tonalite intrusive body encountered at the bottom of the wells in northern Ngatamariki, which likely modified the local stress field in such a way that reverse and strike-slip faulting could occur in close proximity. However, as has been modeled and inferred for the Geysers geothermal field, another high-temperature, naturally fractured reservoir (Jeanne et al., 2015; Martínez-Garzón et al., 2014), injection-induced stress tensor changes are plausible at Ngatamariki.

Fluid injection-induced slip on nearby, suitably oriented fractures is commonly assumed to be the main mechanism responsible for well stimulation. In the Ngatamariki case, however, induced seismicity occurs independently of near-well permeability gain, suggesting that seismic slip and permeability gained through self-propping play a subsidiary role in well stimulation. During the cold-water stimulation test at NM08, injectivity increased rapidly from the start of injection with no apparent sensitivity to the onset of seismicity 10 days later. During injection at NM09, the well was also stimulated but was accompanied by only 11 detected seismic events despite two separate injections totaling >100,000 m^3 of fluid. In the south, interpretation of the cold-water stimulation of well NM10 was complicated by fluid losses during drilling, which induced nearly 140 events but for which no injectivity data exist.

This apparent decoupling of induced seismicity and near-well permeability suggests that slow, aseismic processes dominate well stimulation at Ngatamariki, specifically, and also at other high-temperature, high-permeability geothermal reservoirs where thermoelastic stresses may lead to fracture opening but not necessarily to seismic slip. Other recent studies have raised the possibility that permeability and seismicity need not be related for cases of induced seismicity (e.g., Guglielmi et al., 2015; Riffault et al., 2018; Rinaldi & Rutqvist, 2019), and the data set we present here contributes to the documentation and understanding of this discrepancy.

The degree of decoupling may be a product of the combined high permeability and high temperature of the Ngatamariki reservoir. Lower-temperature resources will not exhibit similar degrees of thermal stimulation, and lower-permeability reservoirs are subject to higher pore pressure perturbations, thus increasing the likelihood of inducing seismicity. However, if permeability enhancement and seismicity are decoupled, as we have shown for Ngatamariki, it may be possible (perhaps through "soft stimulation" techniques Hofmann et al., 2018; Yoon et al., 2014) to design injection operations in similar settings elsewhere in order to achieve the desired permeability gain while limiting the number and magnitude of induced seismic events.

Acknowledgments
We thank the Rotokawa Joint Venture (Tauhara North No. 2 Trust and Mercury NZ Limited) for the funding to conduct this research and for allowing us access to the data and permission to publish our findings. We specifically thank Mohsen Askari and Jonathon Clearwater for their help in accessing and interpreting data from the stimulation of NM09 and the drilling and stimulation of NM10. We also wish to acknowledge the contribution of high-performance computing facilities to the results of this research. New Zealand's national facilities are provided by the NZ eScience Infrastructure (NeSI) and funded jointly by NeSI's collaborator institutions and the Ministry of Business, Innovation & Employment's Research Infrastructure program (https://www.nesi.org.nz). The analysis reported here made use of the ObsPy seismic processing toolbox (Team, 2016), and the matched-filter detection was conducted using the EQcorrscan package (Chamberlain et al., 2017; Chamberlain & Hopp, 2016) which can be freely downloaded and installed via *PyPI* or *Anaconda* on all major platforms. The documentation is hosted at *ReadTheDocs*. We also wish to thank Chris Bromley and an anonymous reviewer for their constructive comments, which greatly improved this manuscript. The final version of the Ngatamariki earthquake catalog can be found at DOI *10.17605/OSF.IO/C2M6U* along with access to the github repository of all scripts used in this work.

References

Allis, R. G. (1982). Mechanism of induced seismicity at the Geysers geothermal reservoir California. *Geophysical Research Letters*, *9*(6), 629–632. Retrieved from https://doi.org/10.1029/gl009i006p00629

Allis, R. G. (2000). Review of subsidence at Wairakei field New Zealand. *Geothermics*, *29*(4-5), 455–478. Retrieved from https://doi.org/10.1029/gl009i006p00629

Allmendinger, R. W., Cardozo, N., & Fisher, D. M. (2011). *Structural geology algorithms: Vectors and tensors*. Cambridge: Cambridge University Press.

Amann, F., Gischig, V., Evans, K., Doetsch, J., Jalali, R., Valley, B., et al. (2018). The seismo-hydromechanical behavior during deep geothermal reservoir stimulations: Open questions tackled in a decameter-scale in situ stimulation experiment. *Solid Earth*, *9*(1), 115–137. Retrieved from https://doi.org/10.5194/se-9-115-2018

Arnold, R., & Townend, J. (2007). A Bayesian approach to estimating tectonic stress from seismological data. *Geophysical Journal International*, *170*(3), 1336–1356. Retrieved from https://doi.org/10.1111/j.1365-246x.2007.03485.x

Bachmann, C. E., Wiemer, S., Goertz-Allmann, B. P., & Woessner, J. (2012). Influence of pore-pressure on the event-size distribution of induced earthquakes. *Geophysical Research Letters*, *39*, L09302. Retrieved from https://doi.org/10.1029/2012gl051480

Baisch, S., Vörös, R., Rothert, E., Stang, H., Jung, R., & Schellschmidt, R. (2010). A numerical model for fluid injection induced seismicity at Soultz-sous-Forêts. *International Journal of Rock Mechanics and Mining Sciences*, *47*(3), 405–413. Retrieved from https://doi.org/10.1016/j.ijrmms.2009.10.001

Bauer, S. J., & Handin, J. (1983). Thermal expansion and cracking of three confined water-saturated igneous rocks to 800°C. *Rock Mechanics and Rock Engineering*, *16*(3), 181–198. Retrieved from https://doi.org/10.1007/bf01033279

Bignall, G (2009). Ngatamariki geothermal field geoscience overview (Tech. Rep.). New Zealand: GNS Science.

Boseley, C., Cumming, W., Urzúa-Monsalve, L., Powell, T., & Grant, M. (2010). A resource conceptual model for the Ngatamariki geothermal field based on recent exploration well drilling and 3D MT resistivity imaging. In *Proceedings world geothermal congress* (pp. 1–8).

Boyle, K., & Zoback, M. (2014). The stress state of the Northwest Geysers California geothermal field, and implications for fault-controlled fluid flow. *Bulletin of the Seismological Society of America*, *104*(5), 2303–2312. Retrieved from https://doi.org/10.1785/0120130284

Bromley, C., Brockbank, K., Glynn-Morris, T., Rosenberg, M., Pender, M., O'Sullivan, M., & Currie, S. (2013). Geothermal subsidence study at Wairakei-Tauhara New Zealand. *Proceedings of the Institution of Civil Engineers - Geotechnical Engineering*, *166*(2), 211–223. Retrieved from https://doi.org/10.1680/geng.12.00040

Buscarlet, E., Moon, H., Wallis, I., & Quinao, J. (2015). Reservoir tracer test at the Ngatamariki geothermal field, pp. 20. Vol. 18.
Cant, J. L., Siratovich, P. A., Cole, J. W., Villeneuve, M. C., & Kennedy, B. M. (2018). Matrix permeability of reservoir rocks Ngatamariki geothermal field, Taupo Volcanic Zone, New Zealand. *Geothermal Energy*, *6*(1), 2. Retrieved from https://doi.org/10.1186/s40517-017-0088-6
Cappa, F., Scuderi, M. M., Collettini, C., Guglielmi, Y., & Avouac, J.-P. (2019). Stabilization of fault slip by fluid injection in the laboratory and in situ. *Science Advances*, *5*(3), eaau4065.
Castellazzi, C., Savage, M. K., Walsh, E., & Arnold, R. (2015). Shear wave automatic picking and splitting measurements at Ruapehu volcano New Zealand. *Journal of Geophysical Research: Solid Earth*, *120*, 3363–3384. Retrieved from https://doi.org/10.1002/2014jb011585
Catalli, F., Rinaldi, A. P., Gischig, V., Nespoli, M., & Wiemer, S. (2016). The importance of earthquake interactions for injection-induced seismicity: Retrospective modeling of the Basel enhanced geothermal system. *Geophysical Research Letters*, *43*, 4992–4999. Retrieved from https://doi.org/10.1002/2016gl068932
Chambefort, I., Buscarlet, E., Wallis, I. C., Sewell, S., & Wilmarth, M. (2016). Ngatamariki geothermal field New Zealand: Geology, geophysics, chemistry and conceptual model. *Geothermics*, *59*, 266–280. Retrieved from https://doi.org/10.1016/j.geothermics.2015.07.011
Chambefort, I., Lewis, B., Wilson, C. J. N., Rae, A. J., Coutts, C., Bignall, G., & Ireland, T. R. (2014). Stratigraphy and structure of the Ngatamariki geothermal system from new zircon U-Pb geochronology: Implications for Taupo Volcanic Zone evolution. *Journal of Volcanology and Geothermal Research*, *274*, 51–70. Retrieved from https://doi.org/10.1016/j.jvolgeores.2014.01.015
Chamberlain, C., & Hopp, C. (2016). EQcorrscan: EQcorrscan v 0.1.3. Retrieved from https://doi.org/10.5281/zenodo.59976
Chamberlain, C. J., Hopp, C. J., Boese, C. M., Warren-Smith, E., Chambers, D., Chu, S. X., et al. (2017). EQcorrscan: Repeating and near-repeating earthquake detection and analysis in Python. *Seismological Research Letters*, *89*, 173–181. Retrieved from https://doi.org/10.1785/0220170151
Clearwater, J., Azwar, L., Barnes, M., Wallis, I., & Holt, R. (2015). Changes in injection well capacity during testing and plant start-up at Ngatamariki. In *World geothermal congress* (pp. 1–11).
Cornet, F. H. (2016). Seismic and aseismic motions generated by fluid injections. *Geomechanics for Energy and the Environment*, *5*, 42–54. Retrieved from https://doi.org/10.1016/j.gete.2015.12.003
Das, I., & Zoback, M. D. (2011). Long-period long-duration seismic events during hydraulic fracture stimulation of a shale gas reservoir. *The Leading Edge*, *30*(7), 778–786. Retrieved from https://doi.org/10.1190/1.3609093
Davidson, J., Siratovich, P., Wallis, I., Gravley, D., & McNamara, D. (2012). Quantifying the stress distribution at the Rotokawa geothermal field, New Zealand. In *Proceedings 34th New Zealand geothermal workshop* (pp. 1–8).
Deichmann, N., & Giardini, D. (2009). Earthquakes induced by the stimulation of an enhanced geothermal system below Basel (Switzerland). *Seismological Research Letters*, *80*(5), 784–798. Retrieved from https://doi.org/10.1785/gssrl.80.5.784
Diehl, T., Deichmann, N., Kissling, E., & Husen, S. (2009). Automatic S Wave picker for local earthquake tomography. *Bulletin of the Seismological Society of America*, *99*(3), 1906–1920. Retrieved from https://doi.org/10.1785/0120080019
Ellsworth, W. L. (2013). Injection-induced earthquakes. *Science*, *341*(6142), 1,225,942. Retrieved from https://doi.org/10.1126/science.1225942
Esaki, T., Du, S., Mitani, Y., Ikusada, K., & Jing, L. (1999). Development of a shear-flow test apparatus and determination of coupled properties for a single rock joint. *International Journal of Rock Mechanics and Mining Sciences*, *36*(5), 641–650. Retrieved from https://doi.org/10.1016/s0148-9062(99)00044-3
Evans, K. F., Genter, A., & Sausse, J. (2005). Permeability creation and damage due to massive fluid injections into granite at 3.5 km at Soultz: 1. Borehole observations. *Journal of Geophysical Research: Solid Earth*, *110*, B04203. Retrieved from https://doi.org/10.1029/2004jb003168
Fang, Y., Wang, C., Elsworth, D., & Ishibashi, T. (2017). Seismicity permeability coupling in the behavior of gas shales CO_2 storage and deep geothermal energy. *Geomechanics and Geophysics for Geo-Energy and Geo-Resources*, *3*(2), 189–198. Retrieved from https://doi.org/10.1007/s40948-017-0051-9
Fehler, M., House, L., Phillips, W., & Potter, R. (1998). A method to allow temporal variation of velocity in travel-time tomography using microearthquakes induced during hydraulic fracturing. *Tectonophysics*, *289*(1–3), 189–201. Retrieved from https://doi.org/10.1016/s0040-1951(97)00315-6
Ge, S., Ellsworth, W., Giardini, D., Townend, J., & Shimamoto, T. (2019). Overseas research advisory committee report on the Pohang earthquake (Tech. Rep.). Republic of Korea: Korean Government Commission on the Cause of the Pohang Earthquake: Overseas Research Advisory Committee.
Ghassemi, A., Tarasovs, S., & Cheng, A.-D. (2007). A 3-d study of the effects of thermomechanical loads on fracture slip in enhanced geothermal reservoirs. *International Journal of Rock Mechanics and Mining Sciences*, *44*(8), 1132–1148.
Ghidaoui, M. S., Zhao, M., McInnis, D. A., & Axworthy, D. H. (2005). A review of water hammer theory and practice. *Applied Mechanics Reviews*, *58*(1), 49–76. Retrieved from https://doi.org/10.1115/1.1828050
Gibbons, S. J., & Ringdal, F. (2006). The detection of low magnitude seismic events using array-based waveform correlation. *Geophysical Journal International*, *165*(1), 149–166. Retrieved from https://doi.org/10.1111/j.1365-246x.2006.02865.x
Grant, M. A., & Bixley, P. F. (2011). *Geothermal reservoir engineering*. Amsterdam: Elsevier. Retrieved from https://doi.org/10.1016/C2010-0-64792-4
Grant, M. A., Clearwater, J., Quinão, J., Bixley, P. F., & Le Brun, M. (2013). Thermal stimulation of geothermal wells: A review of field data. In *Thirty-eighth workshop on geothermal reservoir engineering* (pp. 1–7).
Guglielmi, Y., Cappa, F., Avouac, J.-P., Henry, P., & Elsworth, D. (2015). Seismicity triggered by fluid injection-induced aseismic slip. *Science*, *348*(6240), 1224–1226. Retrieved from https://doi.org/10.1126/science.aab0476
Halwa, L. (2013a). FMI image interpretation report: Might river power Ngatamariki-9 (*Tech. Rep.*) Australia: Schlumberger Oilfield.
Halwa, L. (2013b). Wellbore image interpretation results NM10 (FMI & AFIT - Final) (*Tech. Rep.*) Australia: Schlumberger Oilfield.
Hanks, T. C., & Kanamori, H. (1979). A moment magnitude scale. *Journal of Geophysical Research*, *84*(B5), 2348–2350. Retrieved from https://doi.org/10.1029/jb084ib05p02348
Hofmann, H., Zimmermann, G., Zang, A., & Min, K.-B. (2018). Cyclic soft stimulation (CSS): A new fluid injection protocol and traffic light system to mitigate seismic risks of hydraulic stimulation treatments. *Geothermal Energy*, *6*(1), 27.
Horne, R. (1995). *Modern well test analysis*. Palo Alto, CA: Petroway Inc.
Hsieh, P. A., & Bredehoeft, J. D. (1981). A reservoir analysis of the Denver earthquakes: A case of induced seismicity. *Journal of Geophysical Research*, *86*(B2), 903–920. Retrieved from https://doi.org/10.1029/jb086ib02p00903
Ishibashi, T., Elsworth, D., Fang, Y., Riviere, J., Madara, B., Asanuma, H., et al. (2018). Friction-stability-permeability evolution of a fracture in granite. *Water Resources Research*, *54*, 9901–9918. Retrieved from https://doi.org/10.1029/2018wr022598

Jeanne, P., Rutqvist, J., Dobson, P. F., Walters, M., Hartline, C., & Garcia, J. (2014). The impacts of mechanical stress transfers caused by hydromechanical and thermal processes on fault stability during hydraulic stimulation in a deep geothermal reservoir. *International Journal of Rock Mechanics and Mining Sciences*, *72*, 149–163. Retrieved from https://doi.org/10.1016/j.ijrmms.2014.09.005

Jeanne, P., Rutqvist, J., Rinaldi, A. P., Dobson, P. F., Walters, M., Hartline, C., & Garcia, J. (2015). Seismic and aseismic deformations and impact on reservoir permeability: The case of EGS stimulation at The Geysers California, USA. *Journal of Geophysical Research: Solid Earth*, *120*, 7863–7882. Retrieved from https://doi.org/10.1002/2015jb012142

Kanamori, H., Fujii, N., & Mizutani, H. (1968). Thermal diffusivity measurement of rock-forming minerals from 300° to 1100°K. *Journal of Geophysical Research*, *73*, 595–605. Retrieved from https://doi.org/10.1029/jb073i002p00595

Keranen, K. M., Savage, H. M., Abers, G. A., & Cochran, E. S. (2013). Potentially induced earthquakes in Oklahoma USA: Links between wastewater injection and the 2011 Mw 5.7 earthquake sequence. *Geology*, *41*(6), 699–702. Retrieved from https://doi.org/10.1130/g34045.1

Kissling, E., Ellsworth, W. L., Eberhart-Phillips, D., & Kradolfer, U. (1994). Initial reference models in local earthquake tomography. *Journal of Geophysical Research*, *99*(B10), 19,635–19,646. Retrieved from https://doi.org/10.1029/93jb03138

Krischer, L. (2015). hypoDDpy: hypoDDpy 1.0. Retrieved from https://doi.org/10.5281/zenodo.18907

Kwiatek, G., Martínez-Garzón, P., Dresen, G., Bohnhoff, M., Sone, H., & Hartline, C. (2015). Effects of long-term fluid injection on induced seismicity parameters and maximum magnitude in northwestern part of The Geysers geothermal field. *Journal of Geophysical Research: Solid Earth*, *120*, 7085–7101. Retrieved from https://doi.org/10.1002/2015jb012362

Langenbruch, C., Weingarten, M., & Zoback, M. D. (2018). Physics-based forecasting of man-made earthquake hazards in Oklahoma and Kansas. *Nature Communications*, *9*(1), 3946. Retrieved from https://doi.org/10.1038/s41467-018-06167-4

Langenbruch, C., & Zoback, M. D. (2016). How will induced seismicity in Oklahoma respond to decreased saltwater injection rates? *Science Advances*, *2*(11), e1601542. Retrieved from https://doi.org/10.1126/sciadv.1601542

Langridge, R., Ries, W., Litchfield, N., Villamor, P, Dissen, R. V., Barrell, D., et al. (2016). The New Zealand active faults database. *New Zealand Journal of Geology and Geophysics*, *59*(1), 86–96. Retrieved from https://doi.org/10.1080/00288306.2015.1112818

Lee, H. S., & Cho, T. F (2002). Hydraulic characteristics of rough fractures in linear flow under normal and shear load. *Rock Mechanics and Rock Engineering*, *35*(4), 299–318. Retrieved from https://doi.org/10.1007/s00603-002-0028-y

Lomax, A., Michelini, A., & Curtis, A. (2014). Earthquake location: Direct, global-search methods, *Encyclopedia of complexity and systems science* (pp. 1–33). New York: Springer. Retrieved from https://doi.org/10.1007/978-3-642-27737-5150-2

Lund, B., & Townend, J. (2007). Calculating horizontal stress orientations with full or partial knowledge of the tectonic stress tensor. *Geophysical Journal International*, *170*(3), 1328–1335. Retrieved from https://doi.org/10.1111/j.1365-246x.2007.03468.x

Majer, E. L., Baria, R., Stark, M., Oates, S., Bommer, J., Smith, B., & Asanuma, H. (2007). Induced seismicity associated with enhanced geothermal systems. *Geothermics*, *36*(3), 185–222. Retrieved from https://doi.org/10.1016/j.geothermics.2007.03.003

Martínez-Garzón, P., Bohnhoff, M., Kwiatek, G., & Dresen, G. (2013). Stress tensor changes related to fluid injection at The Geysers geothermal field California. *Geophysical Research Letters*, *40*, 2596–2601. Retrieved from https://doi.org/10.1002/grl.50438

Martínez-Garzón, P., Kwiatek, G., Bohnhoff, M., & Dresen, G. (2017). Volumetric components in the earthquake source related to fluid injection and stress state. *Geophysical Research Letters*, *44*, 800–809. Retrieved from https://doi.org/10.1002/2016gl071963

Martínez-Garzón, P., Kwiatek, G., Sone, H., Bohnhoff, M., Dresen, G., & Hartline, C. (2014). Spatiotemporal changes faulting regimes, and source parameters of induced seismicity: A case study from The Geysers geothermal field. *Journal of Geophysical Research: Solid Earth*, *119*, 8378–8396. Retrieved from https://doi.org/10.1002/2014jb011385

Massiot, C., Lewis, B., & McNamara, D. D. (2012). Interpretation of acoustic borehole images from injection well NM8A, Ngatamariki geothermal field. *GNS Science Consultancy Report 2012*, *192*, 24.

Massiot, C., Nicol, A., McNamara, D. D., & Townend, J. (2017). Evidence for tectonic lithologic, and thermal controls on fracture system geometries in an Andesitic high-temperature geothermal field. *Journal of Geophysical Research: Solid Earth*, *122*, 6853–6874. Retrieved from https://doi.org/10.1002/2017jb014121

Massiot, C., Townend, J., McNamara, D. D., & Nicol, A. (2015). Fracture width and spacing distributions from borehole televiewer logs and cores in the Rotokawa geothermal field, New Zealand. In *World geothermal congress 2015* (pp. 1–12). International Geothermal Association.

McNamara, D. D., Massiot, C., Lewis, B., & Wallis, I. C. (2015). Heterogeneity of structure and stress in the Rotokawa Geothermal Field New Zealand. *Journal of Geophysical Research: Solid Earth*, *120*, 1243–1262. Retrieved from https://doi.org/10.1002/2014jb011480

Mroczek, S., Savage, M., Hopp, C., & Sewell, S. (2016). Shear wave splitting at Rotokawa and Ngatamariki geothermal fields for 2015. In *Proceedings 38th New Zealand geothermal workshop* (Vol. 23, pp. 25).

Mukuhira, Y., Dinske, C., Asanuma, H., Ito, T., & Häring, M. O. (2017). Pore pressure behavior at the shut-in phase and causality of large induced seismicity at Basel Switzerland. *Journal of Geophysical Research: Solid Earth*, *122*, 411–435. Retrieved from https://doi.org/10.1002/2016jb013338

Parotidis, M., Shapiro, S. A., & Rothert, E. (2004). Back front of seismicity induced after termination of borehole fluid injection. *Geophysical Research Letters*, *31*, L02612. Retrieved from https://doi.org/10.1029/2003gl018987

Quinao, J. J., Buscarlet, E., & Siega, F. (2017). Early identification and management of calcite deposition in the Ngatamariki geothermal field, New Zealand. In *Proceedings 42nd workshop on geothermal reservoir engineering* (pp. 1–9).

Riffault, J., Dempsey, D., Karra, S., & Archer, R. (2018). Microseismicity cloud can be substantially larger than the associated stimulated fracture volume: The case of the Paralana enhanced geothermal system. *Journal of Geophysical Research: Solid Earth*, *123*, 6845–6870. Retrieved from https://doi.org/10.1029/2017jb015299

Rinaldi, A. P., & Rutqvist, J. (2019). Joint opening or hydroshearing? Analyzing a fracture zone stimulation at Fenton Hill. *Geothermics*, *77*, 83–98.

Ristau, J. (2009). Comparison of magnitude estimates for New Zealand earthquakes: Moment magnitude, local magnitude, and teleseismic body-wave magnitude. *Bulletin of the Seismological Society of America*, *99*(3), 1841–1852. Retrieved from https://doi.org/10.1785/0120080237

Rubinstein, J. L., & Ellsworth, W. L. (2010). Precise estimation of repeating earthquake moment: Example from Parkfield, California. *Bulletin of the Seismological Society of America*, *100*(5A), 1952–1961. Retrieved from https://doi.org/10.1785/0120100007

Rutledge, J. T., & Phillips, W. S. (2003). Hydraulic stimulation of natural fractures as revealed by induced microearthquakes Carthage Cotton Valley gas field, east Texas. *Geophysics*, *68*(2), 441–452. Retrieved from https://doi.org/10.1190/1.1567214

Schoenball, M., Baujard, C., Kohl, T., & Dorbath, L. (2012). The role of triggering by static stress transfer during geothermal reservoir stimulation. *Journal of Geophysical Research*, *117*, B09307. Retrieved from https://doi.org/10.1029/2012jb009304

Scholz, C. H. (1988). The brittle-plastic transition and the depth of seismic faulting. *Geologische Rundschau*, *77*(1), 319–328. Retrieved from https://doi.org/10.1007/bf01848693

Segall, P. (1989). Earthquakes triggered by fluid extraction. *Geology*, *17*(10), 942. Retrieved from https://doi.org/10.1130/0091-7613(1989)017<0942:etbfe>2.3.co;2

Segall, P., & Fitzgerald, S. D. (1998). A note on induced stress changes in hydrocarbon and geothermal reservoirs. *Tectonophysics*, *289*(1-3), 117–128. Retrieved from https://doi.org/10.1016/s0040-1951(97)00311-9

Sewell, S. M., Addison, S. J., Azwar, L., & Barnes, M. L. (2015). Rotokawa conceptual model update 5 years after commissioning of the 138 MWe NAP plant. In *Proceedings 37th New Zealand geothermal workshop* (pp. 1–8).

Sewell, S., Savage, M., Townend, J., Bannister, S., & Hutchings, L. (2017). Preliminary investigation of seismic velocity variation at the Rotokawa and Ngatamariki geothermal field. In *Proceedings 39th New Zealand geothermal workshop* (pp. 1–13).

Shapiro, S. A., & Dinske, C. (2009). Scaling of seismicity induced by nonlinear fluid-rock interaction. *Journal of Geophysical Research*, *114*, B09307. Retrieved from https://doi.org/10.1029/2008jb006145

Shapiro, S. A., Kummerow, J., Dinske, C., Asch, G., Rothert, E., Erzinger, J., et al. (2006). Fluid induced seismicity guided by a continental fault: Injection experiment of 2004/2005 at the German Deep Drilling Site (KTB). *Geophysical Research Letters*, *33*, L01309. Retrieved from https://doi.org/10.1029/2005gl024659

Shapiro, S. A., Rothert, E., Rath, V., & Rindschwentner, J. (2002). Characterization of fluid transport properties of reservoirs using induced microseismicity. *Geophysics*, *67*(1), 212–220. Retrieved from https://doi.org/10.1190/1.1451597

Shelly, D. R., Beroza, G. C., & Ide, S. (2007). Non-volcanic tremor and low-frequency earthquake swarms. *Nature*, *446*(7133), 305–307. Retrieved from https://doi.org/10.1038/nature05666

Shelly, D. R., Ellsworth, W. L., & Hill, D. P. (2016). Fluid-faulting evolution in high definition: Connecting fault structure and frequency-magnitude variations during the 2014 Long Valley Caldera California, earthquake swarm. *Journal of Geophysical Research: Solid Earth*, *121*, 1776–1795. Retrieved from https://doi.org/10.1002/2015jb012719

Sherburn, S., Sewell, S. M., Bourguignon, S., Cumming, W., Bannister, S., Bardsley, C., et al. (2015). Microseismicity at Rotokawa geothermal field New Zealand, 2008-2012. *Geothermics*, *54*, 23–34. Retrieved from https://doi.org/10.1016/j.geothermics.2014.11.001

Sibson, R. H., & Rowland, J. V. (2003). Stress fluid pressure and structural permeability in seismogenic crust, North Island, New Zealand. *Geophysical Journal International*, *154*(2), 584–594. Retrieved from https://doi.org/10.1046/j.1365-246x.2003.01965.x

Siega, C., Grant, M., Bixley, P., & Mannington, W. (2014). Quantifying the effect of temperature on well injectivity. In *Proceedings 36th New Zealand geothermal workshop* (pp.1–6).

Simone, S. D., Vilarrasa, V., Carrera, J., Alcolea, A., & Meier, P. (2013). Thermal coupling may control mechanical stability of geothermal reservoirs during cold water injection. *Physics and Chemistry of the Earth Parts A/B/C*, *64*, 117–126. Retrieved from https://doi.org/10.1016/j.pce.2013.01.001

Stephens, G., & Voight, B. (1983). Hydraulic fracturing theory for conditions of thermal stress. *International Journal of Rock Mechanics and Mining Sciences & Geomechanics Abstracts*, *20*(2), A34. Retrieved from https://doi.org/10.1016/0148-9062(83)90349-2

Team, T. O. D. (2016). ObsPy 1.0.1. Retrieved from https://doi.org/10.5281/zenodo.48254

Townend, J., Sherburn, S., Arnold, R., Boese, C., & Woods, L. (2012). Three-dimensional variations in present-day tectonic stress along the Australia-Pacific plate boundary in New Zealand. *Earth and Planetary Science Letters*, *353-354*, 47–59. Retrieved from https://doi.org/10.1016/j.epsl.2012.08.003

Trugman, D. T., & Shearer, P. M. (2017). GrowClust: A hierarchical clustering algorithm for relative earthquake relocation with application to the Spanish Springs and Sheldon, Nevada, earthquake sequences. *Seismological Research Letters*, *88*(2A), 379–391. Retrieved from https://doi.org/10.1785/0220160188

Waldhauser, F. (2000). A double-difference earthquake location algorithm: Method and application to the Northern Hayward Fault, California. *Bulletin of the Seismological Society of America*, *90*(6), 1353–1368. Retrieved from https://doi.org/10.1785/0120000006

Walsh, D., Arnold, R., & Townend, J. (2009). A Bayesian approach to determining and parametrizing earthquake focal mechanisms. *Geophysical Journal International*, *176*(1), 235–255. Retrieved from https://doi.org/10.1111/j.1365-246x.2008.03979.x

Watson, A. (2013). Well measurements from completion tests to the first discharge, *Geothermal engineering* (pp. 99–122). New York: Springer. Retrieved from https://doi.org/10.1007/978-1-4614-8569-86

Weber, B., Becker, J., Hanka, W., Heinloo, A., Hoffmann, M., Kraft, T., et al. (2007). SeisComP3—Automatic and interactive real time data processing. In *Geophysical Research Abstracts* (Vol. *9*, No. 09,219).

Wei, S., Avouac, J.-P., Hudnut, K. W., Donnellan, A., Parker, J. W., Graves, R. W., et al. (2015). The 2012 Brawley swarm triggered by injection-induced aseismic slip. *Earth and Planetary Science Letters*, *422*, 115–125. Retrieved from https://doi.org/10.1016/j.epsl.2015.03.054

Wiemer, S. (2000). Minimum magnitude of completeness in earthquake catalogs: Examples from Alaska the western United States, and Japan. *Bulletin of the Seismological Society of America*, *90*(4), 859–869. Retrieved from https://doi.org/10.1785/0119990114

Wiemer, S., & McNutt, S. R. (1997). Variations in the frequency-magnitude distribution with depth in two volcanic areas: Mount St. Helens Washington, and Mt. Spurr, Alaska. *Geophysical Research Letters*, *24*(2), 189–192. Retrieved from https://doi.org/10.1029/96gl03779

Wiemer, S., McNutt, S. R., & Wyss, M. (1998). Temporal and three-dimensional spatial analyses of the frequency-magnitude distribution near Long Valley Caldera California. *Geophysical Journal International*, *134*(2), 409–421. Retrieved from https://doi.org/10.1046/j.1365-246x.1998.00561.x

Wilson, C. J. N., Houghton, B. F., McWilliams, M. O., Lanphere, M. A., Weaver, S. D., & Briggs, R. M. (1995). Volcanic and structural evolution of Taupo Volcanic Zone New Zealand: A review. *Journal of Volcanology and Geothermal Research*, *68*(1-3), 1–28. Retrieved from https://doi.org/10.1016/0377-0273(95)00006-g

Wilson, C. J., & Rowland, J. V. (2016). The volcanic magmatic and tectonic setting of the Taupo Volcanic Zone, New Zealand, reviewed from a geothermal perspective. *Geothermics*, *59*, 168–187. Retrieved from https://doi.org/10.1016/j.geothermics.2015.06.013

Wiprut, D., & Zoback, M. D. (2000). Fault reactivation and fluid flow along a previously dormant normal fault in the northern North Sea. *Geology*, *28*(7), 595–598. Retrieved from https://doi.org/10.1130/0091-7613(2000)028<0595:fraffa>2.3.co;2

Yoon, J. S., Zang, A., & Stephansson, O. (2014). Numerical investigation on optimized stimulation of intact and naturally fractured deep geothermal reservoirs using hydro-mechanical coupled discrete particles joints model. *Geothermics*, *52*, 165–184. Retrieved from https://doi.org/10.1016/j.geothermics.2014.01.009

Zoback, M. D. (2010). *Reservoir geomechanics*. Cambridge: Cambridge University Press.

Zoback, M. D., & Harjes, H.-P. (1997). Injection-induced earthquakes and crustal stress at 9 km depth at the KTB deep drilling site Germany. *Journal of Geophysical Research*, *102*(B8), 18,477–18,491. Retrieved from https://doi.org/10.1029/96jb02814